Absolute proteomic quantification reveals design principles of sperm flagellar chemosensation

Christian Trötschel[1],[*],[§] (ID), Hussein Hamzeh[2,3],[§] (ID), Luis Alvarez[2],[§], René Pascal[2], Fedir Lavryk[2], Wolfgang Bönigk[2], Heinz G Körschen[2], Astrid Müller[2], Ansgar Poetsch[1],[†],[‡],[**] (ID), Andreas Rennhack[2], Long Gui[4], Daniela Nicastro[4], Timo Strünker[2,3,5] (ID), Reinhard Seifert[2,3] & U Benjamin Kaupp[2,3,6],[***] (ID)

Abstract

Cilia serve as cellular antennae that translate sensory information into physiological responses. In the sperm flagellum, a single chemoattractant molecule can trigger a Ca^{2+} rise that controls motility. The mechanisms underlying such ultra-sensitivity are ill-defined. Here, we determine by mass spectrometry the copy number of nineteen chemosensory signaling proteins in sperm flagella from the sea urchin *Arbacia punctulata*. Proteins are up to 1,000-fold more abundant than the free cellular messengers cAMP, cGMP, H^+, and Ca^{2+}. Opto-chemical techniques show that high protein concentrations kinetically compartmentalize the flagellum: Within milliseconds, cGMP is relayed from the receptor guanylate cyclase to a cGMP-gated channel that serves as a perfect chemo-electrical transducer. cGMP is rapidly hydrolyzed, possibly via "substrate channeling" from the channel to the phosphodiesterase PDE5. The channel/PDE5 tandem encodes cGMP turnover rates rather than concentrations. The rate-detection mechanism allows continuous stimulus sampling over a wide dynamic range. The textbook notion of signal amplification—few enzyme molecules process many messenger molecules—does not hold for sperm flagella. Instead, high protein concentrations ascertain messenger detection. Similar mechanisms may occur in other small compartments like primary cilia or dendritic spines.

Introduction

Sensory systems command over exquisite sensitivity and precision. Photoreceptors in the eye can detect single photons (Baylor *et al*, 1979; Yau & Hardie, 2009; Gross *et al*, 2015); chemosensory neurons in the antennae of insects and vomero-nasal organs of mammals can detect a few or even single pheromone molecules (Kaissling, 1986; Leinders-Zufall *et al*, 2000); algae and sperm from marine invertebrates can register single chemoattractant molecules (Boland *et al*, 1982; Starr *et al*, 1995; Kaupp *et al*, 2003). These sensory feats happen in specialized cellular compartments, called cilia or flagella: long, slender filaments that emanate from the cell body (Marshall & Basto, 2017). Cilia and flagella serve as antennae that translate chemical and physical stimuli into electrical signals that eventually evoke a cellular or behavioral response. In recent years, a concept of physiological significance has emerged that cilia and flagella are specialized cell organelles, whose ionic milieu and inventory of signaling proteins are unique (Corbit *et al*, 2005; DeCaen *et al*, 2013; Delling *et al*, 2013; Kaupp & Strünker, 2017; Balbach *et al*, 2018). Factors that may contribute to the exquisite sensory sensitivity of cilia or flagella are the inventory, concentrations, and topographical arrangement of signaling proteins, and the compartmentalization of cellular reactions. How each factor contributes to ultra-sensitivity and plays out in the minuscule reaction volume is largely unknown.

Here, we provide the first absolute quantification of the inventory of a flagellar chemosensory signaling pathway from sperm of the sea urchin *Arbacia punctulata*; this pathway controls chemotactic steering (Kaupp & Strünker, 2017). It is an optimal model system that meets all requirements for reliable absolute quantification. Sperm constitute a homogenous cell population, and flagella can be prepared purely. Moreover, most signaling proteins are

1 Fakultät für Biologie und Biotechnologie, Ruhr-Universität Bochum, Bochum, Germany
2 Center of Advanced European Studies and Research (caesar), Molecular Sensory Systems, Bonn, Germany
3 Marine Biological Laboratory, Woods Hole, MA, USA
4 Departments of Cell Biology and Biophysics, University of Texas Southwestern Medical Center, Dallas, TX, USA
5 Center of Reproductive Medicine and Andrology, University Hospital Münster, Münster, Germany
6 Life& Medical Sciences Institute (LIMES), University of Bonn, Bonn, Germany
*Corresponding author. Tel: +492343224535; E-mail: christian_troetschel@yahoo.de
**Corresponding author. Tel: +4960327051760; E-mail: ansgar.poetsch@rub.de
***Corresponding author. Tel: +49 228 9656 100; Fax: +49 228 9656 9273; E-mail: u.b.kaupp@caesar.de
§These authors contributed equally to this work
†Present address: Center for Marine and Molecular Biotechnology, QNLM, Qindao, China
‡Present address: College of Marine Life Sciences, Ocean University of China, Qingdao, China
[The copyright line of this article was changed on 23 January 2020 after original online publication.]

sperm-specific; therefore, potential contamination by other cell types does not compromise quantification. Importantly, most signaling proteins have been identified—from the chemoattractant receptor to the Ca^{2+} channel that controls chemotactic steering. Absolute mass spectrometric quantification using the QconCAT (quantification concatemers) technology (Scott *et al*, 2016) reveals astoundingly high copy numbers of all 11 signaling proteins in the flagellum. Compared with a typical cell soma, the enzyme-to-substrate ratio is reversed by several orders of magnitude. Using kinetic opto-chemical techniques, we probed the physiological consequences for the dynamics of cellular messengers. Quantification of signaling proteins and cellular responses provides new insights into the molecular underpinnings of chemosensory ultra-sensitivity.

Results

The cGMP-signaling pathway

Chemosensation in the flagellum of sea urchin sperm involves changes in the membrane potential (V_m) and the intracellular concentration of cGMP, cAMP, Na^+, Ca^{2+}, and H^+ (Fig 1A). A

signaling pathway encodes these cellular events (Fig 1B) (for reviews, see; Kaupp & Alvarez, 2016; Wachten *et al*, 2017). The pathway is triggered by *resact*, a chemoattractant peptide that binds to a chemoreceptor guanylate cyclase (GC) and stimulates cGMP synthesis (Garbers, 1976; Singh *et al*, 1988; Kaupp *et al*, 2003; Pichlo *et al*, 2014). The rise of cGMP opens K^+-selective cyclic nucleotide-gated (CNGK) ion channels (Strünker *et al*, 2006; Galindo *et al*, 2007; Bönigk *et al*, 2009). The ensuing hyperpolarization activates a voltage-gated Na^+/H^+ exchanger (sNHE) (Lee, 1985; Windler *et al*, 2018) and a hyperpolarization-activated, cyclic nucleotide-gated (HCN) pacemaker channel (Gauss *et al*, 1998; Galindo *et al*, 2005). Na^+/H^+ exchange increases pH_i, which primes CatSper Ca^{2+} channels to open during the recovery from hyperpolarization probably driven by HCN channels that carry an inward current (Seifert *et al*, 2015; Espinal-Enriquez *et al*, 2017). Changes in free Ca^{2+} concentration ($[Ca^{2+}]_i$) control the swimming path.

The chemoattractant also stimulates cAMP synthesis (Hansbrough & Garbers, 1981; Harumi *et al*, 1992; Kaupp *et al*, 2003), presumably by a soluble adenylate cyclase (sAC) (Vacquier *et al*, 2014). cAMP modulates the activity of sNHE and HCN channels, which both carry a cyclic nucleotide-binding domain (CNBD) (Gauss *et al*, 1998; Wang *et al*, 2003; Windler *et al*, 2018). For signal termination,
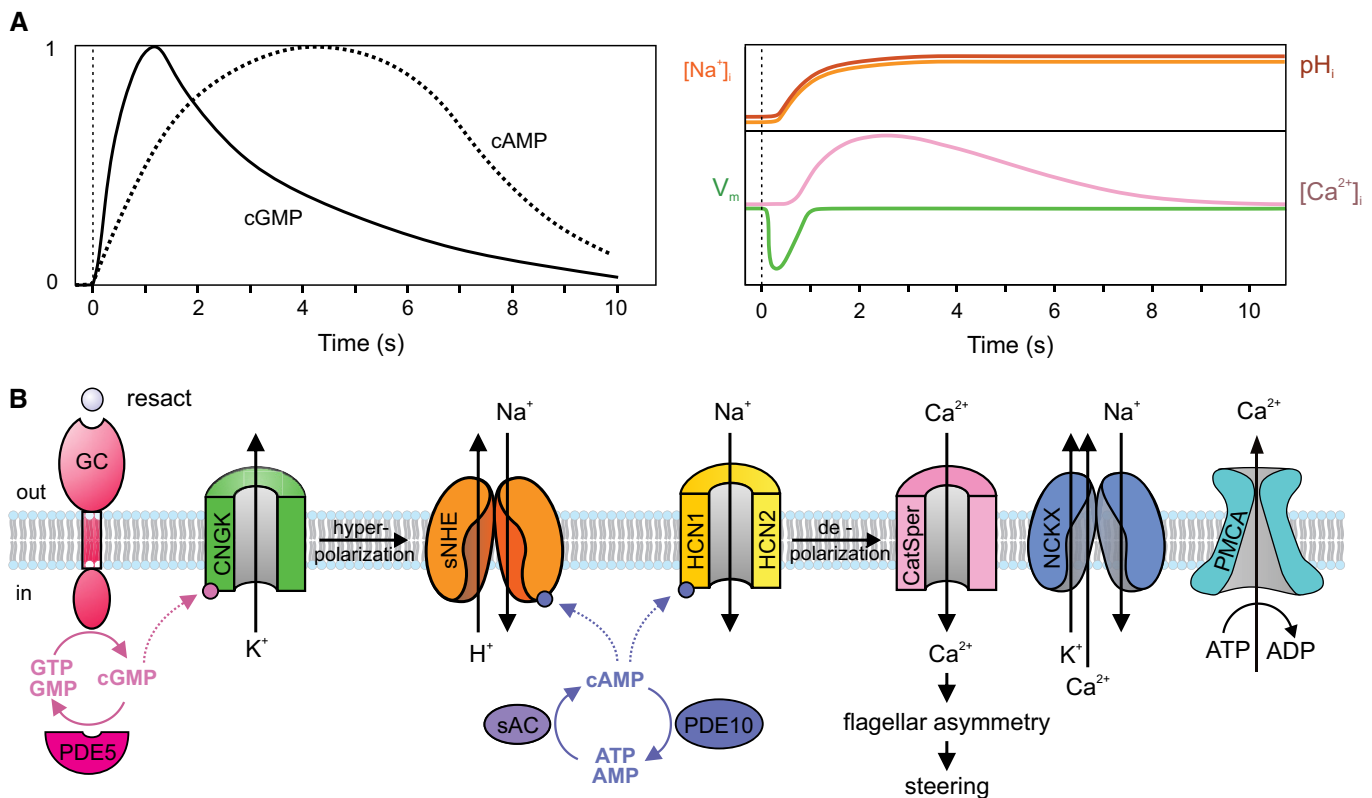

Figure 1. Signaling pathway controlling chemotactic navigation.

A Schematic representation of signaling events. *Left*: time course of changes in cAMP (dotted line) and cGMP (solid line); *right*: time course of changes in V_m (green), pH_i (red); $[Na^+]_i$ (orange), and $[Ca^{2+}]_i$ (pink). Vertical dotted lines indicate time of stimulation.

B GC, receptor guanylate cyclase; CNGK, cyclic nucleotide-gated K^+-selective channel; sNHE (SLC9C1), sperm-specific Na^+/H^+ exchanger; HCN1, HCN2, hyperpolarization-activated, and cyclic nucleotide-gated channels; CatSper, cation channel of sperm; NCKX, $Na^+/Ca^{2+}-K^+$ exchanger; PMCA, plasma membrane Ca^{2+}-ATPase; PDE5, phosphodiesterase type 5; PDE10, phosphodiesterase type 10; sAC, soluble adenylate cyclase. For clarity, sAC is placed in the cytosol, although it is associated with the membrane; the same may apply to PDE10.

a cGMP-specific phosphodiesterase (PDE5) (Su & Vacquier, 2006) breaks down cGMP and, finally, a Na^+/Ca^{2+}-K^+ exchanger (NCKX) (Su & Vacquier, 2002) and/or a plasma membrane Ca^{2+}-ATPase (PMCA) (Gunaratne *et al*, 2006) restore resting Ca^{2+} levels.

Mass spectrometric (MS) analysis of purified flagella from *A. punctulata* sperm identified all previously known signaling components, but also additional proteins that might be involved in the signaling pathway (Appendix Table S1): (i) the Ca^{2+}-activated Cl^- channel TMEM16 of olfactory cilia, which has been predicted to exist in sperm from pharmacological and modeling studies (Guerrero *et al*, 2013; Espinal-Enriquez *et al*, 2017); (ii) a dual-specific PDE10 that, unlike PDE5, can also hydrolyze cAMP, and, together with sAC, may control cAMP metabolism; (iii) K^+/Cl^- co-transporters KCC1 (*SLC12A4*) and/or KCC3 (*SLC12A5*); (iv) a Na^+/HCO_3^- co-transporter (*SLC4A11*); (v) a sperm-specific Na^+/K^+-ATPase α subunit; and (vi) two members (TMC 5 and 7) of a mechano-sensitive channel family (Zhao & Müller, 2015; Pan *et al*, 2018). Sperm respond to mechanical stimulation with a Ca^{2+} response (Kambara *et al*, 2011). The TMC channels may endow sperm with mechano-sensitivity. Using antibodies directed against their mammalian homologues, several transmembrane adenylate cyclases (tmAC 1, 2, 5, and 9) were detected in sea urchin sperm (Beltrán *et al*, 2007; Vacquier *et al*, 2014). Although we identified 45 different peptides for sAC, we could not detect peptides for tmACs.

For absolute quantification, we selected 11 signaling proteins shown in Fig 1B along with their subunits, a total of 19 polypeptides (Appendix Table S2). The newly discovered proteins molecules, except for PDE10 and Na^+/K^+-ATPase, were not considered for absolute quantification because their function in chemotactic signaling remains to be elucidated.

Absolute quantification by QconCAT technology

The abundance of proteins was quantified by selected reaction monitoring (SRM) using a synthetic, isotope-labeled protein as a standard (Rivers *et al*, 2007; Brownridge *et al*, 2011; Holman *et al*, 2012). For the synthesis of the standard protein, we selected three individual tryptic peptides from most of the 19 signaling proteins; a few proteins were covered by two or four peptides (Appendix Table S2). The presence of the peptides after trypsin digestion of the standard protein was verified by both MALDI-TOF and LC-ESI-MS/MS (SRM). These control experiments failed to retrieve three peptides (Appendix Table S2), which, therefore, were not used for quantification. Consequently, quantification of NCKX and CatSper3 rested on a single peptide, which might underestimate the protein abundance. For absolute quantification, we used the receptor GC, the most abundant protein of the flagellar membrane, as a reference protein. Previous work determined 200,000–400,000 GC molecules/flagellum by quantitative SRM (using a PSAQ-GC as a standard) (Pichlo *et al*, 2014), Coomassie Blue densitometry (Pichlo *et al*, 2014), and high-resolution electron tomography (Farci, 2017). We consider the GC density determined by electron tomography as the most precise estimate. Therefore, protein copy numbers were[#] calculated assuming 400,000 GC molecules (Table 1); all protein ratios from SRM analyses are given in Dataset Table EV1. Moreover,

as another internal benchmark of quantification, we included creatine kinase (CK) that, according to gel densitometry, is almost as abundant as the receptor GC (Pichlo *et al*, 2014). By SRM, we observed a GC:CK ratio close to unity, underscoring the high accuracy and suitability of using a synthetic labeled protein for MS determination of protein stoichiometries.

Determination of flagellar volume by cryo-electron tomography

For comparison, we calculated protein concentrations from copy numbers in the flagellum. The total volume inside motile cilia and flagella (V_t) contains three distinct compartments: the matrix volume (V_{ma}) that is accessible to diffusing or transported ciliary proteins, the volume occupied by the [9 + 2] axonemal scaffold (V_a), and the lumen (V_l) of the nine doublet microtubules and the two singlet microtubules of the central pair complex. The microtubules are only accessible to small molecules like ions, nucleotides, and ligands (e.g., Taxol) (Fig 2). Thus, $V_t = V_{ma} + V_a + V_l$, and the volume accessible to small molecules is $V_{asm} = V_{ma} + V_l$ (Fig 2F′ and F″). We measured these volumes using cryo-electron tomography reconstructions of rapidly frozen flagella for two evolutionary distant species, i.e., from the unicellular green algae *Chlamydomonas reinhardtii* and from sperm of the sea urchin *Strongylocentrotus purpuratus* (Carbajal-Gonzalez *et al*, 2013; Lin & Nicastro, 2018; preprint: Fu *et al*, 2019; Lin *et al*, 2019) (Fig 2A–D).

For calculating the V_t, we measured the mean diameter (d) of intact flagella for *Chlamydomonas* as 247 ± 13 nm and for sea urchin sperm as 266 ± 13 nm (Fig 2E). Thus, the mean V_t per 1-μm flagellar length is for *Chlamydomonas* 0.0479 μm³ and for sea urchin sperm 0.0557 μm³; i.e., for an average length of sea urchin flagella of 40 μm, the total volume V_t is 2.2 fl (see Materials and Methods section for details). Overall, the sub-volumes per 1-μm flagellar length were very similar between the two species (Table 2). We used the matrix volume (for 40 μm long *S. purpuratus* flagella) $V_{ma} = 1.7$ fl to calculate protein concentrations in Table 1. Surprisingly, volumes accessible to proteins (V_{ma}) and small molecules (V_{asm}) are 77 and 86% of the total volume.

Signaling proteins are orders of magnitude more abundant than free messengers

To compare protein abundance, Table 1 lists copy numbers, protein concentrations, and the densities of integral membrane proteins. We find that signaling proteins in the flagellum (Fig 1B) are up to 1,000-fold more abundant than the respective cellular messengers like H^+, Ca^{2+}, cAMP, and cGMP (Table 1). For example, the flagellum harbors 21,700 CNGK channels that are key targets of cGMP. Each CNGK channel is activated by a single molecule of cGMP (Bönigk *et al*, 2009), and, at low and moderate chemoattractant stimulation of sperm, only ten to a few hundred cGMP molecules are synthesized by the receptor GC (Bönigk *et al*, 2009; Pichlo *et al*, 2014). The large number of CNGK channels suggests that this stage of signal transduction, i.e., capturing of cGMP, is highly efficient. The downstream targets of the CNGK channel, sNHE exchangers and HCN channels (Fig 1B) that are activated by hyperpolarization, are

---

[#]Correction added on 27 January 2020, after first online publication: "stoichiometry was" has been changed to "copy numbers were".

Table 1. Copy number, concentration, and membrane density of signaling proteins.

Proteins	Molecules/Flagellum[a]	Concentration[b] (µM)	Density[c] (molecules/µm²)
GC	400,000	400	11,976
CNGK	21,653 ± 4,038	21.7 ± 4	648
sNHE	53,979 ± 20,659	54 ± 20.7	1,616
sAC	6,718 ± 2,630	6.7 ± 2.6	201
HCN1	10,258 ± 901	10.3 ± 0.9	307
HCN2	18,337 ± 887	18.3 ± 0.9	549
CatSper1	1,853 ± 147	1.9 ± 0.1	56[d]
CatSper2	2,125 ± 138	2.1 ± 0.1	
CatSper3[e]	587 ± 296	0.6 ± 0.3	
CatSper4	1,208 ± 113	1.2 ± 0.1	
CatSper β	1,690 ± 547	1.7 ± 0.5	
CatSper γ	1,169 ± 1,395	1.2 ± 1.4	
CatSper δ	2,071 ± 392	2.1 ± 0.4	
PDE5	48,567 ± 6,525	48.6 ± 6.5	
PDE10	4,211 ± 752	4.2 ± 0.8	
NCKX[e]	120,795 ± 41,520	120.8 ± 41.5	3,617
Ca²⁺-ATPase	1,991 ± 749	2 ± 0.7	60
Na⁺/K⁺-ATPase	48,280 ± 16,788	48.3 ± 16.8	1,446
Creatine Kinase	364,465 ± 29,428	364.5 ± 29.4	10,912

[a]Mean ± SD from six animals.
[b]Calculated from column 2, assuming a matrix volume V_{ma} of 1.7 femtoliter.
[c]Calculated from column 2, assuming a flagellar surface area of 33.4 µm² (r = 0.133 µm; l = 40 µm); only membrane-bound proteins are considered.
[d]Mean calculated from all CatSper subunits, except CatSper3, assuming a 1:1 stoichiometry of subunits.
[e]Data from a single peptide only.

present at 54,000 and 28,000 molecules per flagellum, respectively. Remarkably, the sNHE is not involved in pH homeostasis at rest; only upon chemoattractant stimulation, it tightly couples membrane voltage and cAMP to generate rapid alkalization (latency < 300 ms) that is necessary for CatSper channel activation (Seifert *et al*, 2015; Windler *et al*, 2018). In mammalian sperm, sAC exists as a full-length form (sAC$_{fl}$; 180 kDa) and a truncated form (sAC$_t$; 55 kDa). We chose four peptides, two from sAC$_t$ and two from sAC$_{fl}$ to estimate the relative abundance of each form. All four peptides occurred at similar frequencies, suggesting that only full-length sAC exists in sea urchin sperm. Approximately 1,700 CatSper channels generate a rise of [Ca²⁺]$_i$, and a remarkably high number of 120,000 NCKX exchanger proteins subsequently clear the flagellum from Ca²⁺ and restore the resting state. Because the time derivative of the Ca²⁺ response modulates the flagellar beat (Alvarez *et al*, 2012), tightly balanced Ca²⁺ influx and efflux are key to successful navigation. Finally, we determined 48,600[§] PDE5 molecules and 4,200 PDE10 molecules, which hydrolyze cGMP and cAMP, respectively, and terminate chemotactic signaling. In summary, the concentrations of signaling proteins range from 2 to 400 µM, whereas their respective substrates cAMP, cGMP, protons, and Ca²⁺ are present at much lower free concentrations.

The prodigiously high copy numbers of signaling proteins raise several paradigmatic questions about signaling in ciliary compartments. How does the high density affect the speed and efficacy of signaling at each stage along the transduction pathway? Does the high density confine signaling events to the flagellum? Do signaling proteins serve as buffers for messengers? In the following, using opto-chemical techniques, we address these questions experimentally and assess the results by theory and numerical simulation. Thereby, we gain mechanistic insight into the physiological network of chemotactic signaling.

Tracking of cGMP by the CNGK channel and PDE5

The CNGK-mediated hyperpolarization is the first key signaling event; when hyperpolarization is abolished, downstream events are forestalled (Harumi *et al*, 1992; Pichlo *et al*, 2014; Seifert *et al*, 2015). For maximum efficacy, the CNGK channel must capture any cGMP molecule before it is wasted by hydrolysis or diffusion to the sperm head. Using rapid-mixing techniques and flash photolysis of caged cGMP (Hamzeh *et al*, 2019), we addressed two questions: How fast and efficiently does the CNGK channel entrap cGMP molecules, and how fast is the channel cleared from cGMP by PDE5 hydrolysis?

As read-out for cGMP dynamics, we recorded the CNGK-mediated V_m changes using fluorescent potentiometric indicators FluoVolt and Di-8-ANEPPS, which detect changes in V_m by photo-induced electron
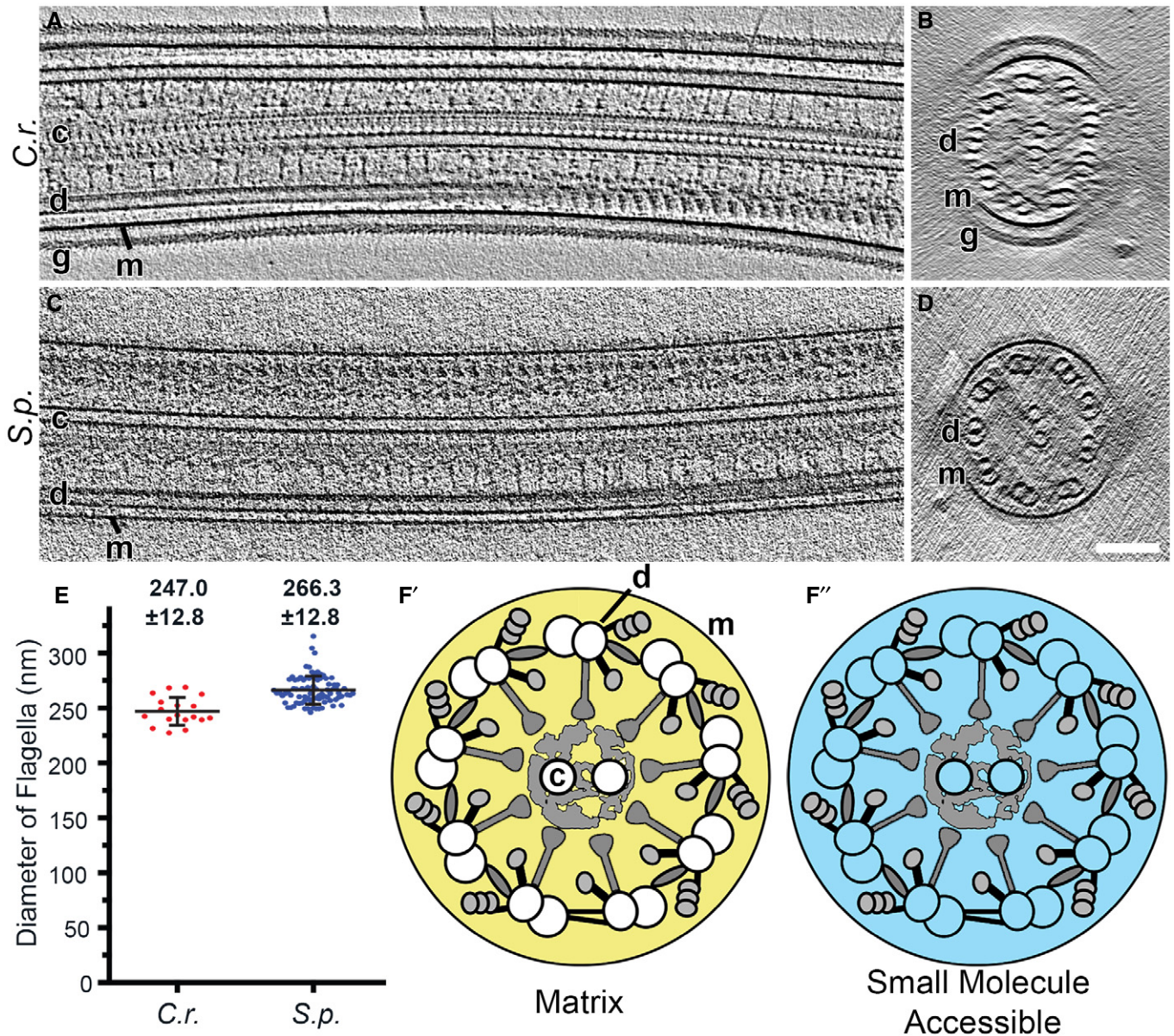
Figure 2. Determination of flagellar volumes.

A–D   Longitudinal (A and C, proximal view on left) and cross-sectional (B and D, proximal-to-distal view) tomographic slices of representative intact flagella from wild-type *Chlamydomonas reinhardtii* (*C.r.*) flagella (A and B) and sea urchin *Strongylocentrotus purpuratus* (*S.p.*) sperm (C and D). Note that in *Chlamydomonas*, the flagellar membrane (m) is surrounded by a glycocalyx (g). Other labels: central pair complex (c) and doublet microtubule (d). Scale bar, 100 nm.

E   Diameter of intact flagella from *Chlamydomonas* and sea urchin sperm measured on cross-sectional views of cryo-tomographic reconstructions. Numbers indicate average diameters ± SD ($n = 84$ for sea urchin (*S.p.*) and $n = 18$ for *Chlamydomonas* (*C.r.*)).

F′, F″   Schematic diagrams of *Chlamydomonas* flagella in cross-sectional view. The yellow area (F′) indicates the matrix volume V_{ma} that is accessible to proteins, and the cyan area (F″) represents the volume that is accessible to small molecules V_{asm} (i.e., the combination of the matrix volume and the microtubule lumen).

transfer (PeT) and electrochromism, respectively. For the physiological cGMP-induced hyperpolarization, this read-out is likely contaminated by opening of HCN channels that carry a depolarizing inward Na^+ current (Gauss *et al*, 1998). Therefore, we recorded V_m in the presence of 100 mM external $[K^+]_o$ (100KASW), which clamps the reversal potential V_{rev} for CNGK to approximately -37 mV, i.e., more positive than the resting voltage V_{rest} of approximately -50 mV (Strünker *et al*, 2006; Seifert *et al*, 2015). Consequently, at

high $[K^+]_o$, CNGK opening should depolarize rather than hyperpolarize sperm. At $V_m > -37$ mV, the open probability of HCN channels is low, and HCN channels are unlikely to contribute much to V_m (Gauss *et al*, 1998). Furthermore, high $[K^+]_o$ abolishes changes in pH_i, $[Ca^{2+}]_i$, and cAMP evoked by the chemoattractant or cGMP (Pichlo *et al*, 2014; Seifert *et al*, 2015); therefore, putative pH-, Ca^{2+}-, or cAMP-regulated conductances, like HCN channels, are unlikely to interfere with changes in V_m evoked by CNGK activity.

Table 2. Diameter and volumes[a] of flagella from the green alga *Chlamydomonas reinhardtii* and of sperm from the sea urchin *Strongylocentrotus purpuratus*.

	d[b]	V_{ma}	V_a	V_l	V_{asm}	V_t
C. reinhardtii	247 ± 13	3.66/76.3	0.70/14.6	0.43/9.1	4.09/85.4	4.79/100
S. purpuratus	266 ± 13	4.31/77.4	0.81/14.5	0.45/8.1	4.76/85.5	5.57/100

[a]Sub-volumes in $\times 10^{-2}$ μm^3/percentage of total volume V_t.
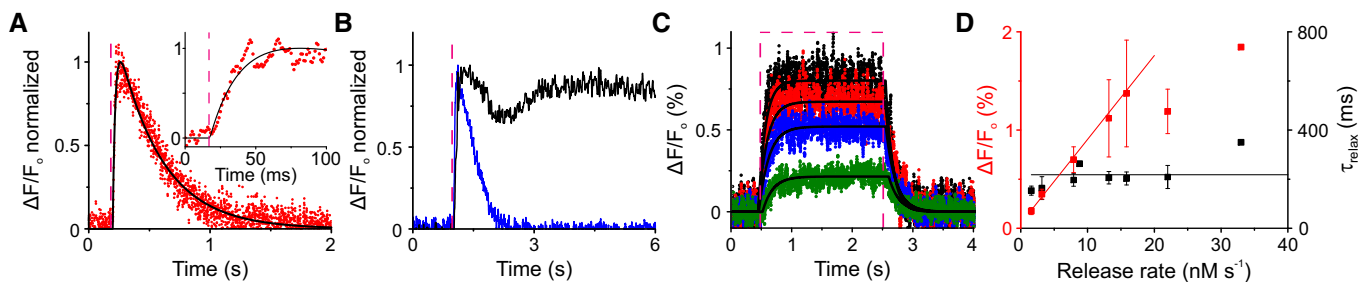[b]Flagellar diameter d in nm.

Sperm were loaded with DEACM-caged cGMP. This neutral hydrophobic compound readily equilibrates across the cell membrane; therefore, photorelease of cGMP inside cells can be calibrated precisely. Changes in V_m were followed with the voltage-sensitive PeT dye FluoVolt (Miller *et al*, 2012; Hamzeh *et al*, 2019). Sperm were rapidly mixed in a stopped-flow apparatus with 100KASW and then stimulated with a brief flash of light that photo-released cGMP. A 2-ms flash (releasing 52 nM of cGMP) gave rise to an almost instantaneous depolarization that relaxed to baseline levels in < 1 s (Fig 3A). A fit of the rise and relaxation of the V_m signal using equation (1) (in Materials and Methods—data analysis and simulations) yielded time constants $\tau_{rise} = 16.6 \pm 7.3$ ms and $\tau_{relax} = 384 \pm 107$ ms ($n = 3$ experiments) (Fig 3A). The mean τ_{rise} is compatible with estimates of the rate of cGMP binding to CNGK ($\tau_{binding} = 1$–2 ms) or the RC time constant of the membrane (5–20 ms), which represent lower bounds of τ_{rise} (Materials and Methods section).

Because CNGK channels are not voltage dependent and do not desensitize in the presence of cGMP (Bönigk *et al*, 2009), the relaxation time τ_{relax} might reflect the closure of CNGK due to the removal of cGMP. We tested this presumption using a DEACM-caged form of 8-Br-cGMP (Hagen *et al*, 2003), a hydrolysis-resistant analogue that also activates CNG channels (Zimmerman *et al*, 1985; Kaupp & Seifert, 2002). Release of 8-Br-cGMP by a light flash evoked a rapid depolarization that, by contrast to cGMP, was persistent and did not relax—except for a small transient dip (Fig 3B). The 8-Br-cGMP experiment shows that cGMP hydrolysis is ultimately required for closure of CNGK channels and rapid recovery of V_m.

What limits the rate of cGMP hydrolysis: the rate of cGMP dissociation from CNGK or the catalytic power of PDE5? We determined the V_m/light energy relation using 2-s light pulses over a 50-fold range of light energies. Invariably, during the light pulse, V_m rose to a stable plateau that was graded with increasing light energy (Fig 3C and D), suggesting that PDE5 is exactly counterbalancing steady cGMP release. The steady-state amplitude of ΔV_m increased linearly for low light energies, consistent with the idea that PDE5 is constitutively active (Rybalkin *et al*, 2003) (Fig 3C and D). At the end of a light pulse, V_m returned to V_{rest} with a characteristic time τ_{relax} that was constant for a 50-fold range of cGMP-photolysis rates and that was similar to τ_{relax} of signals evoked by short light flashes (220 ms vs. 384 ms) (Fig 3C). The independence of τ_{relax} from cGMP levels suggests that dissociation of cGMP from CNGK determines the rate of V_m recovery rather than PDE5's catalytic power. We scrutinized this notion by mathematical calculation and numerical simulations.

Estimates of cGMP turnover kinetics

We calculated the V_m recovery kinetics for three different reaction schemes (Fig 4A) (see Materials and Methods section and Appendix). Scheme 1 involves the CNGK channel alone; scheme 2 involves the PDE alone; and scheme 3 involves CNGK and PDE together, recapitulating the *in vivo* situation. Schemes assume that cGMP must first dissociate from CNGK before PDE5 can degrade it. Therefore, the rate of cGMP dissociation provides an upper bound for τ_{relax}. The calculated dissociation rate is $k_{off} = 0.68/s$ or

Figure 3. Dynamics of CNGK activation and cGMP hydrolysis.

A Time course of the change in voltage V_m evoked by a 2-ms light flash in sperm that was loaded with caged cGMP (15 μM) and recorded in 100KASW. Inset: extended timescale showing the rise of V_m. Fit of data (black) using two exponentials with time constants $\tau_{rise} = 17.4$ ms and $\tau_{relax} = 354$ ms. Light flash in all panels is depicted as dashed magenta line.

B Time course of the changes in V_m evoked by 100-ms flash in 100KASW using caged cGMP (blue) and caged 8-Br-cGMP (black). The flashes released 260 nM cGMP or 2,600 nM 8-Br-cGMP.

C Time course of changes in V_m in 100KASW evoked by 2-s flashes at different light energy that corresponds to 440, 220, 75, and 8 nM/s of cGMP. Data were fitted using a heuristic model described by equation (3) (Materials and Methods section) (black lines).

D Amplitude (red) and decay time τ_{relax} (black) for different light energies and release rates for experiments as shown in panel C. τ_{relax} was determined using a single exponential fit. The linear fit of the V_m amplitude was restricted to low light levels; at higher levels, the V_m response saturates (see panel C). Points indicate mean ± SD from five experiments.
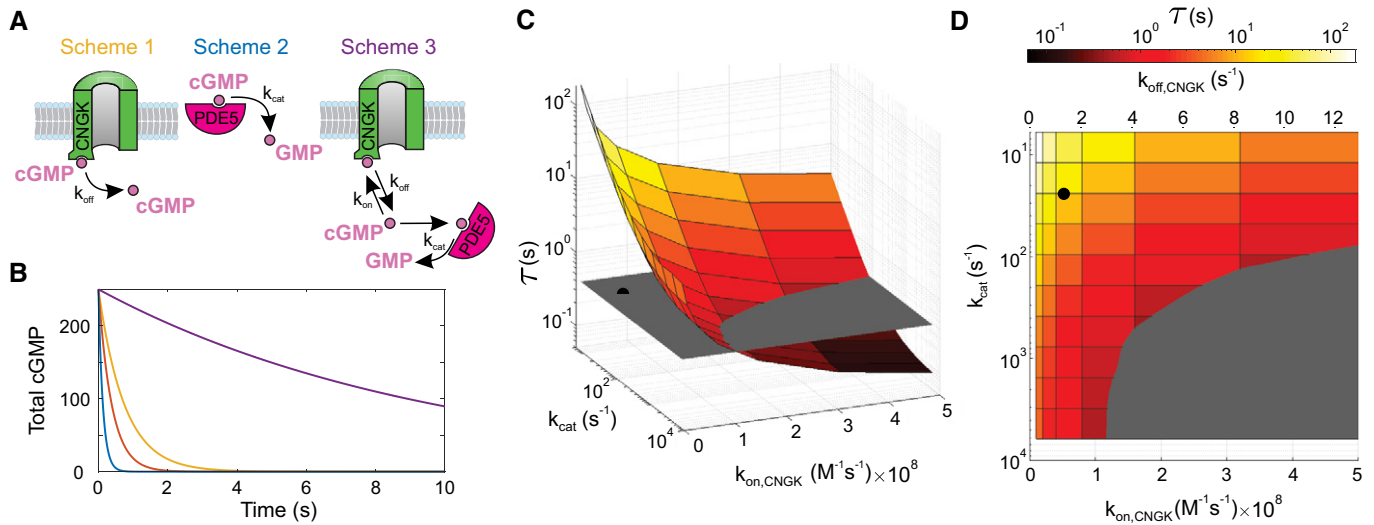
Figure 4. Discrete-event simulations of cGMP dynamics.

A   Schemes illustrate three different situations defined by chemical reactions (2) to (5) in the Materials and Methods section. Colors of schemes refer to the simulations shown in panel (B).

B   Characteristic decay of V_m in experiments shown in Fig 3A and C (orange; τ_{relax} = 0.384 s) is compared with cGMP hydrolysis by PDE5 in the absence of CNGK channels (blue; characteristic time τ = 0.131 s), dissociation of cGMP from CNGK at the rate k_{off} (yellow; τ = 0.748 s), and cGMP hydrolysis in the presence of CNGK channels and PDE (violet; τ = 9.73 s). Simulations were done using those parameters listed in Appendix Table S3. cGMP is given in molecules.

C   Simulations of the rate of cGMP hydrolysis upon varying the catalytic rate k_{cat} of active PDE and the k_{on} rate of cGMP binding to the CNBD of the CNGK channel. The gray plane indicates the experimental relaxation time (τ_{relax}). The black dot represents k_{cat} (24/s) and k_{on} (5.2 × 10^7/M/s) compatible with previous studies (Appendix Table S3). The pairs of parameters compatible with the experimental τ_{relax} are positioned at the intersection of the colored surface and the gray plane.

D   Top view of panel C showing k_{off} values compatible with k_{on} rates used for simulations (assuming $K_{D,CNGK}$ = 25.7 nM; see Appendix Table S3).

τ_{off} = 1.48 s, assuming a k_{on} = 2.6 × 10^7/M/s and a constant of half-maximal activation $K_{1/2}$ = 2.6 × 10^{-8} M (Bönigk *et al*, 2009; Peuker *et al*, 2012). Accounting for the effect of ionic strength on second-order rate constants (Peuker *et al*, 2012) and assuming that the ionic strength of seawater and the cytosol is similar, k_{on} rates might be twofold larger (k_{on} = 5 × 10^7/M/s; τ_{off} = 0.75 s) (Fig 4B). Intriguingly, the shortest estimate of τ_{off} is about twofold to fourfold longer than experimental τ_{relax} for V_m recovery.

Second, we estimated a lower bound for τ_{relax} if the turnover number k_{cat} of PDE5 were rate-limiting (Fig 4A, PDE alone). For constitutively active PDE5 (k_{cat} = 24/s and N_{PDE5} = 48,600), the time constant of cGMP hydrolysis was estimated to be 131 ms (Materials and Methods section) (Fig 4B). Thus, the hydrolytic power of PDE5 is not rate-limiting.

Finally, we simulated cGMP hydrolysis under *in vivo* conditions, i.e., in the presence of both PDE5 and CNGK. In this scenario, cGMP hydrolysis was considerably slowed down (τ = 9.6 s) (Fig 4B), primarily due to rebinding of cGMP to the high-affinity site of CNGK. We searched the parameter space for values of k_{cat} (PDE) and k_{on}/k_{off} (CNGK) that are compatible with experimental τ_{relax} (Fig 4C). To achieve τ_{relax}, high values for both k_{on} (CNGK) and k_{cat} (PDE5) are required (Fig 4D, gray area). Such high k_{on} and k_{cat} values have not been observed for CNBD domains and for sea urchin or mammalian PDE5, respectively (Kaupp *et al*, 2003; Rybalkin *et al*, 2003). In conclusion, given the high CNGK concentration and the high k_{on} value, hydrolysis of cGMP free in solution, for a wide range of parameters, fails to explain the extraordinary fast cGMP breakdown. To solve this conundrum, we propose substrate "channeling" between CNGK and PDE as a mechanism

that might accelerate cGMP dissociation from the channel and, ultimately, hydrolysis (see Discussion).

Simulations provided additional insight regarding the potential role of the allosteric GAF-A domain that is conserved in *A. punctulata* PDE5. Mammalian PDE5 displays basal activity that is about threefold enhanced by binding of cGMP to the GAF-A domain (Rybalkin *et al*, 2003). The cGMP-stimulated activity scheme yielded the same kinetics as the basal activity-only scenario: For physiological stimulation levels, the enhanced activity of a few PDE5 molecules is negligibly small compared with the basic activity of ten thousand of active PDE5 molecules. Although GAF-A domains display a relatively high cGMP affinity (K_D ~200 nM; Francis *et al*, 2011), they do not compete with CNGK or the catalytic PDE domain for cGMP, because its k_{on} is almost 1,000- and 100-fold lower than k_{on} for cGMP binding to the CNGK channel and to the catalytic PDE5 domain, respectively (Appendix Table S3). Thus, putting the kinetic argument aside, even at equilibrium, the CNGK channel captures ≥ 90 % of cGMP molecules.

Control of V_m recovery by HCN channels

In many cells, HCN channels counteract hyperpolarization and, thereby, serve several different functions. In the retina, HCN channels extend the frequency response and operational light range of rod and cone photoreceptors (Fain *et al*, 1978; Barrow & Wu, 2009). In neurons and heart cells, HCN channels sustain oscillatory activity and modulate resting V_m (Pape, 1996). In sperm, the precise function of HCN channels has been elusive. Two different HCN channel subunits (HCN1 and HCN2) exist in sea urchin sperm (Gauss *et al*, 1998; Galindo *et al*, 2005). Do these subunits form homomeric or

heteromeric channels? What is their physiological function? We detected in the flagellum 10,000 and 18,000 copies of HCN1 and HCN2 channel subunits, respectively. Do HCN channels counteract the chemoattractant-induced hyperpolarization? We compared the rate of V_m recovery after weak and strong cGMP stimulation, i.e., when HCN channel activity is low and high, and for both depolarizing (100KASW) and hyperpolarizing (ASW) responses. For strong hyperpolarization, V_m completely recovered within 110 ms, while a large fraction of CNGK channels was still open (Fig 5A, compare blue and red traces). Thus, HCN channels clearly outperform CNGK channels. For weak stimuli, i.e., for small depolarization or hyperpolarization, the V_m response relaxed with similar time constants of about 300 ms (Fig 5A, compare pink and navy traces). The 1.5-fold larger amplitude of the hyperpolarizing compared with the depolarizing signal is due to the larger electrochemical driving force. We systematically determined the recovery time over a wide range of stimulus strength (Appendix Fig S1A). The recovery time was similar (τ_{relax} = 280 ms) (Fig 5B inset) when ρ 30 cGMP molecules

(equivalent to ≤ 3 chemoattractant molecules) were produced, and hastened gradually with increasing hyperpolarization, i.e., HCN channel activation (Fig 5B). In conclusion, HCN channels accelerate recovery—except for weak stimuli.

We scrutinized this conclusion by inhibiting either cGMP hydrolysis or HCN activity. The relaxation times of hyperpolarizing responses evoked by photolysis of caged 8-Br-cGMP or caged cGMP were similar (Fig 5C), except for a depolarizing overshoot. Similarly, inhibition of PDE activity by high concentrations of IBMX (1 mM) did not retard recovery (Fig 5D). The depolarizing voltage overshoot was abolished either in the absence of Ca^{2+} (Fig 5D) or when 8-Br-cGMP was used as a stimulus (Fig 5C), suggesting that recovery is first driven by a Na^+ inward current carried by HCN channels, followed by Ca^{2+} currents carried by CatSper channels. Finally, inhibition of the HCN channels by the drug ZD7288 (Postea & Biel, 2011) strongly slowed down recovery (Fig 5E and F). In the presence of the drug, V_m signals also became smaller (Fig 5E), because the drug also shifted V_{rest} to more negative values, which compressed the
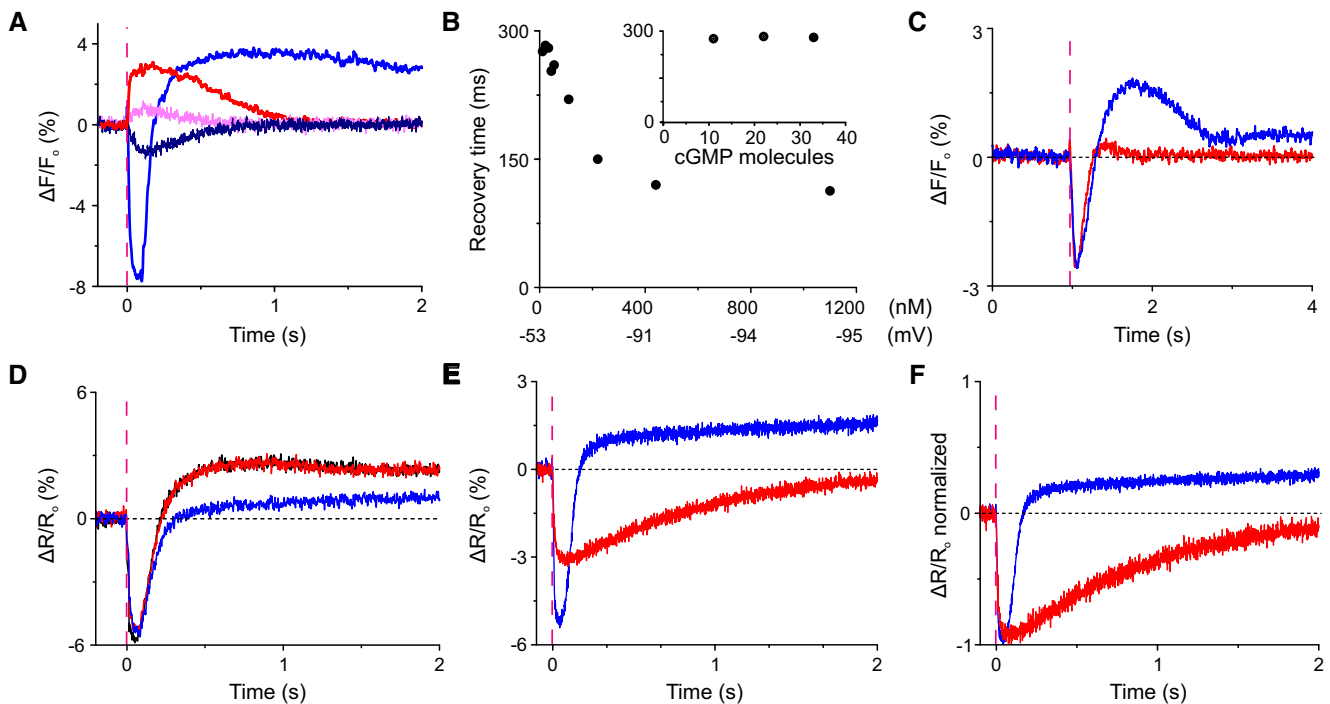

Figure 5. Recovery from hyperpolarization[$].

A Time course of cGMP-evoked changes in V_m in 100KASW (red, 500 nM cGMP; pink, 9 nM cGMP) and normal ASW (blue, 500 nM cGMP; navy, 9 nM cGMP). The time constants of recovery after cGMP release (9 nM) were 289 ms (depolarization) and 303 ms (hyperpolarization). Signals in panels (A–C) were detected using the potentiometric probe FluoVolt; dashed magenta lines indicate the timing of the photolysis flash.
B Representative measurement of the dependence of recovery-time constant on the amount of released cGMP. Inset: Decay time was constant for low stimulation levels equivalent to ≤ 30 cGMP molecules or ≤ 3 resact molecules.
C Voltage response evoked by photolysis of DEACM-caged cGMP (blue) or 8-Br-cGMP (red). The light energy was adjusted such that V_m response amplitudes became similar; for 8-Br-cGMP, about five times more light energy was required. Light pulse 10 ms.
D cGMP-evoked V_m response in ASW (black), in the presence of IBMX (1 mM) (red), and in Ca^{2+}-free ASW ([Ca^{2+}] ≤ 500 nM) in the presence of IBMX (1 mM) (blue). Signals in panels (D–F) were detected using the potentiometric probe Di-8-ANEPPS in the ratio mode.
E V_m responses evoked by cGMP in the presence (blue) and absence (red) of the HCN channel blocker ZD7288 (50 μM).
F Normalized responses from panel (E).

operational range of hyperpolarization (Appendix Fig S1B). Of note, in the presence of ZD7288, the recovery time is similar to that at 100KASW, i.e., in the absence of HCN channel activity. Collectively, these results show that except for low stimulation levels, HCN channel activation controls the time of recovery from hyperpolarization.

Components of Ca²⁺ signaling

Three different signaling proteins control Ca^{2+} homeostasis: the Ca^{2+} channel CatSper, a NCKX exchanger, and a Ca^{2+}-ATPase (Fig 1B). Their quantitative stoichiometry provides several insights. First, CatSper in mammalian sperm comprises four homologous pore-forming subunits (CatSper 1-4) (Navarro *et al*, 2008) and at least five auxiliary subunits (CatSper β, γ, δ, ε, and ζ) (Liu *et al*, 2007; Wang *et al*, 2009; Chung *et al*, 2011, 2017). CatSper1-4, β, γ, and δ were also detected in *Arbacia* sperm (Seifert *et al*, 2015). Except for CatSper3, each of the subunits was equally abundant, suggesting that each subunit contributes one copy to a large CatSper complex. The CatSper 3 quantification relied on one peptide only; thus, the estimate is less reliable than for the other CatSper subunits.

Second, the NCKX exchanger is one of the most abundant signaling molecule, only second to the receptor GC (Table 1). By contrast, the PMCA pump is 50-fold less abundant, showing that $Na^+/Ca^{2+}/K^+$ exchange is the major if not only mechanism of Ca^{2+} clearance from the flagellum. In fact, PMCA is more abundant in the head than the flagellum (Gunaratne *et al*, 2006). The NCKX exchanger is also about 50-fold more abundant than the CatSper channel. This high ratio is required because of the vastly different transport numbers of ion channels and ion exchangers: Ca^{2+} channels can carry > 1,000 ions/s (Hille, 2004), whereas NCKX exchangers can transport about 100–300 Ca^{2+} ions/s (Jalloul *et al*, 2016).

NCKX transporters use inward Na^+- and outward K^+ gradients for Ca^{2+} extrusion (Cervetto *et al*, 1989; Schnetkamp, 2013). The exchange is electrogenic ($4Na^+$:$1Ca^{2+}$:$1K^+$) and therefore enhanced at negative membrane potentials (Cervetto *et al*, 1989). The involvement of Na^+- and K^+ gradients and the electrogenic mechanism suggests rapid ion-exchange kinetics and very low Ca^{2+} levels at rest. NCKX is primarily expressed in sensory neurons, in particular in rod and cone photoreceptors (Schnetkamp *et al*, 2014). The resting $[Ca^{2+}]_i$ in rods is 100 nM and, during hyperpolarization, can reach levels as low as 5–10 nM (Woodruff *et al*, 2002). We assume that $[Ca^{2+}]_i$ in sperm can also adopt such low levels.

Third, its high density argues that NCKX can restore basal Ca^{2+} levels in the flagellum before Ca^{2+} diffuses to the head compartment. We tested this presumption by recording cGMP-evoked Ca^{2+} changes, using the fluorescent Ca^{2+} indicator GFP-certified FluoForte, in the flagellum and the head separately. A flash of light, producing 28 cGMP molecules (equivalent to approximately 3 resact molecules), evoked a short Ca^{2+} pulse in the flagellum, but no significant change in the head (Fig 6A). For stronger stimulation, a small delayed Ca^{2+} signal in the head became apparent (Fig 6B). In conclusion, for low stimulation levels, the Ca^{2+} response is restricted to the flagellum; for higher stimulus strengths, the signal partially propagates from the flagellum to the head.

Changes in pH_i are compartmentalized

A voltage-activated Na^+/H^+ exchanger (SLC9C1 or sNHE) is the only molecule known in sperm to regulate pH_i. Its exquisitely high density

(Table 1) explains why changes in pH_i occur on a millisecond time scale (Seifert *et al*, 2015; Windler *et al*, 2018). We examined whether cGMP-evoked changes in pH_i, similar to Ca^{2+} signals, are restricted to the flagellum. Changes in pH_i were measured, using the fluorescent pH indicator pHrodo Red, in the flagellum and the head separately (Fig 6C and D). The pH_i rose rapidly in the flagellum and declined again within 3 s (Fig 6C). By contrast, the alkalization in the head was much smaller and slower. After about 4 s, the pH_i in flagellum and head was equal and slightly elevated. This result is consistent with the idea that Na^+/H^+ exchange in the flagellum elevates pH_i (Windler *et al*, 2018) and that this change slowly propagates to the head.

Discussion

In a typical cell soma, signaling proteins are less or about equally abundant than their respective substrates; processing of many substrate molecules by a single active enzyme lies at the heart of cellular signal amplification. For example, in the ERK and AKT pathways concentrations of signaling proteins range between 10 and 1,000 nM (Adlung *et al*, 2017). By contrast, the enzyme-to-substrate ratio in the sperm flagellum is reversed: Signaling proteins are up to 1,000-fold more abundant (micromolar range) than their free substrates (nanomolar range). Simply put, a large number of enzymes, transporters, and channels compete for few substrate molecules, and a single enzymatic turnover by a minute fraction of signaling proteins suffices to initiate or upend a cell response. Clearly, this minuscule reaction vessel is designed for a specific purpose: low-noise, perfect molecule detection rather than signal amplification.

The high-affinity CNGK channel acts as a close-to-perfect cGMP detector that avidly adsorbs cGMP molecules and translates binding events into an incremental voltage response. Binding happens faster than spreading of cGMP along the flagellum by unrestricted diffusion (about 1 s) (Pichlo *et al*, 2014). Furthermore, PDE5 is unlikely to kinetically compete for cGMP binding. Thus, the single-molecule sensitivity of sperm ultimately rests not only on the exquisitely high density and affinity of the receptor GC (Pichlo *et al*, 2014), but also on the CNGK channel as well.

The target proteins of cAMP, Ca^{2+}, and H^+ are also orders of magnitude more abundant than the free messengers themselves. The high density serves two different functions. Rapid sequestering of cellular messengers attenuates their diffusional exchange between flagellum and head. Kinetic compartmentalization enhances antennal sensitivity and shields acrosomal exocytosis in the head, which is also controlled by cAMP, Ca^{2+}, and pH_i (Buffone, 2016), from signaling events in the flagellum. In addition, the time derivative of the Ca^{2+} response d$[Ca^{2+}]_i$/dt rather than absolute $[Ca^{2+}]_i$ determines the curvature of the swimming path (Alvarez *et al*, 2012). Therefore, kinetic control of the Ca^{2+} influx/efflux balance is key to chemotactic navigation. Transport rates of solute carriers are orders of magnitude slower than those of ion channels. The 60-fold higher NCKX density compared with CatSper ascertains that the Ca^{2+} rise can be rapidly counterbalanced. The same argument holds for Na^+/H^+ exchange by sNHE that, within milliseconds, can alkalize the flagellum—a key event that primes Ca^{2+} entry (Seifert *et al*, 2015; Windler *et al*, 2018).

Slow dissociation of cGMP from its high-affinity site at CNGK is at odds with fast 380-ms cGMP turnover. This discrepancy is reminiscent of a similar conundrum about cAMP recycling in the protein
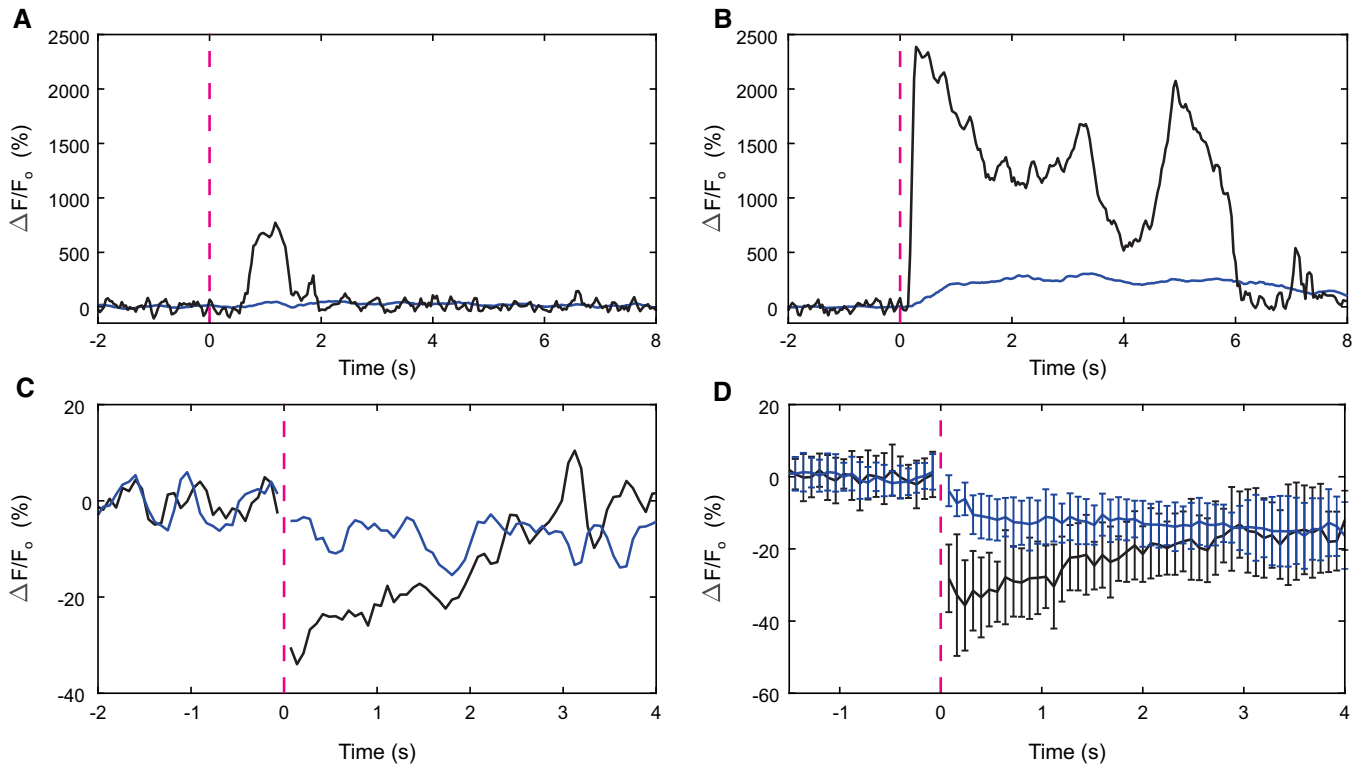
Figure 6. Compartmentalization of Ca2+ and pHi signals. Changes in relative fluorescence ∆F/F recorded from the head and the flagellum are shown in blue and black, respectively.

A, B   Ca2+ signals elicited by cGMP release and recorded with FluoForte. The UV flash released 28 (A) and 215 B) cGMP molecules. Light flashes are indicated by dashed magenta lines.

C   pHi signals, elicited by the release of approximately 1,400 cGMP molecules, were recorded with pHrodo Red. An increase in pHi is indicated by a decrease in ∆F/F. Exemplary recording from a single cell.

D   Average of pHi signals recorded from n = 25 cells. Error bars represent SD See Appendix Fig S2 for a longer time course.

kinase A (PKA) system. The regulatory subunit R binds cAMP with extremely high affinity (K_D = 2–10 nM); consequently, cAMP recycling is expected to be slow. The decade-long riddle (Ramirez-Sarmiento, 2017) was recently unraveled by proposing a "substrate-channeling" mechanism: cAMP, PDE8, and RIα form a ternary complex; cAMP is transferred between active sites of RIα and PDE8 by restricted diffusion without release into the cytosol (Krishnamurthy *et al*, 2014, 2015; Ramirez-Sarmiento, 2017; Tulsian *et al*, 2017). The allosteric active-site coupling tweaks cAMP dissociation from RIα and, thereby, accelerates hydrolysis. Notably, PDE8 is only active in the RIα-cAMP-PDE8 complex (Tulsian *et al*, 2017), a mechanism that prevents breakdown of free cAMP. Two lines of evidence suggest that CNGK and PDE5 form a similar "channeling" complex (Fig 7A): cGMP turnover is much faster than estimated from reaction kinetics in free solution, and the CNGK/PDE5 ratio is 1:1 (assuming PDE5 forms dimers via the GAF-B domain; Francis and Corbin (2010)). Future work needs to establish this mechanism for PDE5. The "channeling" mechanism renders cGMP binding to CNGK essentially irreversible; before cGMP has a chance to dissociate, it is hydrolyzed. Within the framework of chemosensation physics (Berg & Purcell, 1977; Endres & Wingreen, 2008), the inner surface of the flagellar membrane constitutes a perfect absorber rather than a monitoring surface that allows dissociation and rebinding of a ligand. The sensing precision of a perfect absorber is 2.5-fold enhanced compared with a monitoring surface (Endres & Wingreen, 2008).

A far-reaching consequence of rapid cGMP binding to CNGK and "channeling" to PDE5 is that the mean resting-free cGMP concentration is almost zero and that the cGMP action happens on the membrane surface rather than the cytosol. Several back-of-the-envelope estimates illustrate this conclusion. The free cGMP concentration is determined by the rates of synthesis and hydrolysis. To maintain a free cGMP concentration of 1 nM (equivalent to one cGMP molecule/flagellum) in the face of a basal hydrolysis rate of 2.6/s requires the synthesis of 2,103 cGMP molecules/s by 210 active GC molecules/s (calculated from a turnover rate of 72 cGMP/s/GC and a lifetime of 150 ms of active GC; Pichlo *et al* (2014)). Such basal activity would be equivalent to 30 pM of the chemoattractant; at this concentration, 210 chemoattractant molecules/s hit the flagellum; Berg, 1993; Pichlo *et al*, 2014). When PDE activity is blocked, the resting cGMP level should rise to high micromolar concentrations. In fact, elevated cGMP levels were not observed in such experiments (Kaupp *et al*, 2003), arguing that non-stimulated GC activity at rest is negligible. Moreover, such high background activity would seriously compromise if not abolish single-molecule detection of sperm. For comparison, single-photon sensitivity in rod photoreceptors is limited by spontaneous thermal activation of roughly one rhodopsin molecule/min (Luo *et al*, 2011). Finally, at chemical equilibrium with
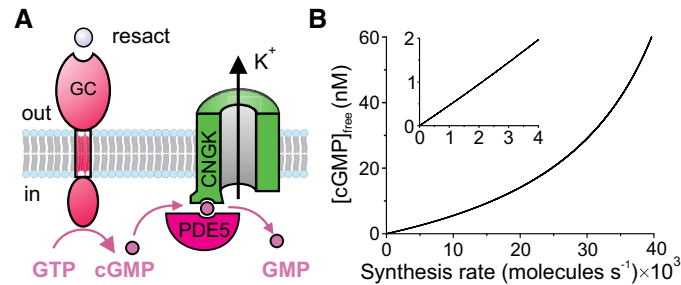
Figure 7. Channeling model of cGMP turnover.

A   cGMP molecules synthesized by the GC receptor rapidly bind to the CNGK channel. CNGK, PDE5, and cGMP form a ternary complex, and cGMP bound to CNGK is subsequently transferred to PDE5 for hydrolysis without being released to the cytosol.

B   Relationship between cGMP synthesis rate and free cGMP concentration. We assume that a single GC molecule can synthesize 10 cGMP molecules during its lifetime of 150 ms (Pichlo *et al*, 2014). Inset: expanded scale.

1 nM free cGMP, approximately 800 cGMP molecules are bound to CNGK channels [calculated from K_D = 26 nM (Bönigk *et al*, 2009) and c_{CNGK} = 22 μM; Table 1)]. Because binding of a single cGMP molecule can open CNGK (Bönigk *et al*, 2009), 800 CNGK channels would be permanently open at rest. By comparison, the opening of maximally 300 CNGK channels by the chemoattractant saturates the V_m response (Strünker *et al*, 2006). In conclusion, free cGMP concentration is virtually zero at rest.

We propose that the GC/CNGK/PDE5 triad is designed to encode rates of cGMP production rather than free cGMP concentrations. Over a 40,000-fold range of cGMP synthesis rates, the free cGMP concentration increases almost linearly (Fig 7B). Of note, even for strong stimulation, a rate-encoding mechanism never saturates the CNGK channel with cGMP and allows cells to operate over a wide dynamic range. Another important benefit of rate-detection is the speed with which a cell response can be initiated: No binding equilibrium has to be reached, and no diffusional times have to be awaited. A cell can rapidly and continuously sample a stimulus landscape and respond in real time. The mechanism is optimal to probe a chemical gradient on periodic paths with 1–2 Hz frequency.

Finally, our study also illustrates fundamental limits to track cellular messenger concentrations in small compartments using genetically encoded or chemical sensors. The sensitivity of available cAMP/cGMP sensors (ranging between 70 nM; Mukherjee *et al* (2016) and 3 μM; Halls and Canals (2018)) would be not sufficient to detect changes in free cyclic nucleotide concentrations in sperm. Enhancing a sensor's ligand affinity creates another dilemma because sensors become inherently slow and are expected to seriously interfere with the *in situ* kinetics and steady-state concentrations of messengers. These challenges are exacerbated in primary cilia (volume about 0.2 fl), where one cAMP molecule is equivalent to 10-nM concentration, and a single molecule of adenylate cyclase can produce 100 cAMP molecules/s (equivalent to 1 μM/s). Using intrinsic sensors as read-out for cAMP/cGMP signaling combined with quantitative photonic control of cAMP/cGMP, as shown here, may overcome this fundamental problem.

The mechanisms of kinetic compartmentalization of cilia seem to depend on the nature of the messenger. The porous cilia base allows small proteins to freely enter or exit the cilium (Kee *et al*, 2012; Breslow *et al*, 2013). Accordingly, Ca^{2+} ions can freely diffuse from the primary cilium into the cell soma. Nevertheless, the ciliary

$[Ca^{2+}]$ is threefold to fivefold higher than that in the soma (DeCaen *et al*, 2013; Delling *et al*, 2013). The high concentration is maintained by Ca^{2+}-permeant channels in the cilia membrane despite steady Ca^{2+} diffusion into the cytoplasm at the ciliary base (Delling *et al*, 2013). Thus, the kinetic balance of Ca^{2+} entry and exit determines ciliary Ca^{2+} levels. Considering that the soma volume is up to 50,000-fold larger than the ciliary volume, the steady Ca^{2+} flux into the soma does not change the cytosolic $[Ca^{2+}]_i$ appreciably.

In a model of the cAMP-regulated sonic hedgehog (Hh) pathway, cAMP leaves the cilium and activates PKA at the ciliary base or in the soma (Mukhopadhyay & Rohatgi, 2014). However, a recent study using proximity-labeling MS identifies several cAMP-signaling proteins in cilia of IMCD-3 cells (Mick *et al*, 2015), including AC5, AC6, and $RI_α$ and $RII_β$ subunits of PKA, suggesting that activation of the transcription factors GLI2 and GLI3 by PKA phosphorylation occurs inside the cilium during transient visits of the respective targets (Mick *et al*, 2015). The absolute and relative abundance of ciliary ACs and PKA is largely unknown (for a comprehensive discussion see Mick *et al*, 2015). The ciliary free cAMP concentration reportedly is high (4 μM), i.e., fivefold higher than in the soma of embryonic fibroblasts (Moore *et al*, 2016). How such high concentrations can be reconciled with a PKA sensitivity of < 10 nM cAMP remains enigmatic. We envisage that similar scenarios of high-abundance signaling proteins, kinetic compartmentalization, substrate-channeling, and reaction-rate sensing may endow primary cilia with exquisite sensitivity, speed, and a wide dynamic range. Rigorous quantification of signaling repertoires combined with rapid photonic techniques, as outlined here, may provide unprecedented insights not only for ciliary signaling, but also for other small subcellular compartments like neuronal dendrites and spines.

Materials and Methods

Preparation of flagella

The collection of *A. punctulata* sperm and the preparation of flagella were as described in Seifert *et al* (2015) with one modification: Instead of shearing with a 24-G needle, the sperm suspension was sheared 20 times by centrifugation for 30 s at 75× *g* and 4°C through a 40-μm mesh of a cell strainer (BD Biosciences, USA). Flagella were

washed in artificial seawater (ASW), containing (in mM): 423 NaCl, 9.27 $CaCl_2$, 9 KCl, 22.94 $MgCl_2$, 25.5 $MgSO_2$, 0.1 EDTA, and 10 HEPES, adjusted to pH 7.8 with NaOH, and stored as pellet.

Analysis of solubilization efficacy by Coomassie staining and Western blotting

The precise determination of copy numbers and protein stoichiometries relies on the efficacy of protein solubilization by detergents. Therefore, we tested for different solubilization conditions the fraction of proteins in the supernatant and the pellet by SDS–PAGE and Western blotting of selected membrane-associated proteins (Appendix Fig S3). Flagella were resuspended in solubilization buffer [10 mM Tris–HCl, pH 7.6; 140 mM NaCl, 1 mM EDTA, 1% dodecyl-maltopyranoside (DDM), protease inhibitor cocktail 1:500 (P8340, Sigma-Aldrich, USA)]. The protein concentration determined by BCA assay was 1.5 µg/µl. The solubilizate was split into three samples for parallel incubation. Tubes 1 and 2 were incubated on ice for 30 min, and tube 3 was incubated on ice for 120 min. Flagella in tube 2 were sonicated three times for 30 s (Sonifier 450, Branson, Danbury, CT). After incubation, supernatant and pellet were separated by centrifugation ($10,000\times g$ at 4°C).

To compare the different solubilization conditions, proteins in the supernatant and pellet were separated on a 7.5% SDS gel for Coomassie staining or on an 8% SDS precast gel (SurePAGE, Genscript, NJ, USA) for Western blotting. Each lane was loaded with the equivalent of 8 µg of flagellar protein. Pre-stained Protein Marker VI (AppliChem, Darmstadt, Germany) was used as molecular weight marker.

Proteins were transferred onto an Immobilon FL PVDF membrane (Merck Millipore, Darmstadt, Germany) and consecutively probed with various antibodies. After each probing, the Western blot was analyzed using the Odyssey Imaging System (LI-COR, Bad Homburg, Germany). All figure panels were taken from the same Western blot. Figures were prepared using CorelDraw X6 and Photo-Paint X6 software (both from Corel Corporation). Primary antibodies were monoclonal: rat GCN 3D10 (anti-GC, 1:200) (Pichlo et al, 2014), polyclonal rabbit ETK rb1 (anti-ApsAC, 1:200), monoclonal rat ApNHE 14E1 (anti-NHE, 1:200), monoclonal rat AP47G4 (anti-ApCNGK (repeat 4), 1:20) (Bönig et al, 2009), and monoclonal mouse α-tubulin B-5-1-2; (1:5,000, Sigma, T5168). Antibodies have been produced in rat (monoclonal) or rabbit by the Helmholtz Zentrum München (German Research Center for Environmental Health, Monoclonal Antibody Core Facility, Germany) and LifeTein (Somerset, NJ, USA), respectively. Secondary antibodies were as follows: anti-rat or anti-rabbit IRDye680 antibody (1:25,000, red channel) and anti-rat or anti-mouse IRDye800 antibody (1:25,000, green channel) from LI-COR.

The major integral membrane protein, the receptor guanylate cyclase (GC), and the equally abundant membrane-associated creatine kinase (CK) were almost completely transferred to the supernatant. For the GC, we estimated that < 10% remained in the pellet (Appendix Fig S3A). A similar result was obtained for the soluble adenylate cyclase (sAC), the CNGK channel, and the Na^+/H^+ exchanger (sNHE) (Appendix Fig S3B). The proteins in the pellet were largely axonemal proteins, e.g., tubulin (55 kDa) and an intermediate chain of the motor protein dynein (75 kDa). Furthermore, copy number ratios in the DDM-extracted supernatant were compared with ratios in flagella solubilized in DDM plus SDS-sample buffer. Except for PDE10, these ratios were similar within

experimental error (Appendix Table S4). In conclusion, for quantitative MS, aliquots of flagella from six animals were resuspended and incubated for 30 min on ice in solubilization buffer. After centrifugation at $10,000\times g$ and 4°C, the supernatant was transferred to a new tube.

Selection of candidate peptides for protein quantification

Candidate peptides were identified from previous data using MudPIT and one-dimensional sodium dodecyl sulfate–polyacrylamide gel-electrophoresis followed by liquid chromatography (GeLC-MS) (Seifert et al, 2015). For MudPIT, flagella were washed twice with 0.1 M $(NH_4)_2CO_3$ and sedimented by ultracentrifugation ($100,000\times g$, 30 min, 4°C). Membrane pellets were resuspended, sonicated, and processed by tryptic in-solution digestion (sequencing grade-modified trypsin, Promega) in a methanol and NH_4HCO_3 buffer (Fischer & Poetsch, 2006). After removal of membranes by ultracentrifugation, samples were desalted using Spec PT C18 AR tips (Varian). For GeLC-MS, 45 µg flagella protein was loaded on a 10% SDS–PAGE gel. The gel was stained with colloidal Coomassie G-250, then destained with acetic acid and the separation gel divided into 12 pieces. Each piece was cut into gel cubes and digested (Pichlo et al, 2014) with 6.25 ng/µl trypsin in a NH_4HCO_3 buffer (20 mM at pH 8.6). Spectra obtained from GeLC-MS and MudPIT were searched against the latest target sequences (to be published) using SEQUEST algorithm, embedded in Proteome Discoverer™ (Rev. 1.4.1.14, Thermo Fisher Scientific, USA). The mass spectrometry proteomics data have been deposited to the ProteomeXchange Consortium via the PRIDE (Perez-Riverol et al, 2019) partner repository with the dataset identifier PXD015332. Additionally, an in silico prediction using Skyline software (Version 3.7) (MacLean et al, 2010) was performed to complete the list of candidate peptides for quantification. Only peptides without methionine, cysteine, and without arginine or lysine motifs like KK, KR, RK, or RR were validated in subsequent SRM measurements of A. punctulata sperm flagella. The 53 most suitable peptides (Table 2) were selected for quantification of the 19 polypeptides involved in chemotactic signaling. The corresponding ^{13}C, ^{15}N Arg/Lys-labeled QconCAT standard protein (M_w 65.42 kDa; concentration: 1.22 mg/ml; 15.2 nmol/mg) was designed and custom-synthesized by PolyQuant GmbH (Germany). Importantly, the isotope-labeled protein was used to confirm the identity of the previously selected 53 peptides by manual pairwise comparison of retention times during LC and by comparison of fragment ions of the respective sample and standard peptides. For three peptides, no correct light/heavy pairs were observed; these peptides were excluded from quantitative analysis (Table 2). Ultimately, 50 peptides were used for protein quantification.

Quantification of chemotaxis signaling proteins by selected reaction monitoring (SRM) mass spectrometry

For quantification, an aliquot of 20 µg sperm flagella protein was spiked with either 0.15, 1.5, or 15 pmol isotope-labeled standard protein to account for different concentrations of sperm target proteins. The standard protein/sample mixtures were subjected to 12.5% (v/v) SDS–PAGE. The SDS–PAGE was stopped after the sample had migrated about 1 cm into the separation gel, and the gel was stained with Coomassie Blue. The about 1-cm-long gel piece was cut into 1–2 mm-sized pieces. In-gel digestion was performed

as described (Pichlo *et al*, 2014) with 6.25 ng/µl trypsin in a NH_4HCO_3 buffer (40 mM at pH 8.6).

The LC-MS/MS system consisted of a TSQ Vantage Triple Quad MS (Thermo Fisher Scientific, USA) interfaced with a nanoAcquity UHPLC system (Waters, USA). LC used an Acquity UPLC M-Class Symmetry C18 trap column (5 µm particle size, 180 µm × 20 mm, 2D, V/M) and an Acquity UPLC M-Class HSS T3 analytical column (1.8 µm particle size, 75 µm × 150 mm) (Waters, USA). LC conditions (66-min multistep gradient from 1 to 99% acetonitrile/0.1% formic acid at a flow rate of 0.4 µl/min) were as described (Pichlo *et al*, 2014). SRM parameters for the TSQ Vantage and data analysis with Skyline 3.7 were as described (Pichlo *et al*, 2014) with the following changes: The two most intense and specific fragment ions (transitions) were used for quantification, and a measuring time window of ± 2.5 min from each peak apex and a 3-s cycle time were set. For optimal ion transmission, the following S-lens RF values were fixed: 53 at 182.082 *m/z*, 109 at 508.208 *m/z*, and 220 at 997.398 *m/z*. The collision energy was first predicted by Skyline 3.7 and then individually optimized for each precursor ion. Heavy-isotope incorporation was determined by in-solution digestion of the standard protein, followed by SRM analysis as described above. Heavy-isotope incorporation was 97% (arginine) and 98% (lysine).

Calculation of copy numbers and statistical analysis

All SRM data were manually inspected to ensure correct peak identification. Furthermore, from three different amounts of 0.15, 1.5, or 15 pmol standard protein per 20 µg flagella protein, individual L/H ratios were selected to exclude extreme values. The peak area of each light (sperm sample) and heavy standard peptide was calculated using Skyline 3.7 and exported to an Excel sheet for further data processing. The total area of each heavy peptide was corrected for the percentage of heavy-isotope incorporation. For example:

Total area heavy		Heavy-isotope incorporation		Total area heavy corrected
5,558,109	/	0.971	=	5,724,108

The total area of each light peptide was corrected for the percentage of light-isotope incorporation in the isotope-labeled standard protein:

Total area light		Total area heavy corrected		Light-isotope incorporation		Total area light corrected
556,239	–	(5,724,108	*	0.029)	=	390,240

The ratios between the corrected peak areas of each light and heavy peptide were calculated using Excel. Based on these ratios, the numbers of molecules of the light peptides were calculated using Avogadro's number. For the different peptides assigned to the same protein, the median and the standard deviation were calculated. For each replicate, the ratios between the different proteins, e.g., guanylate cyclase-to-creatine kinase ratio, and the mean ± SD of all replicates belonging to the same animal were calculated. Representative results are presented in Dataset Table EV2, and the underlying RAW files and Skyline analyses have been made publicly available at

ProteomeXchange with identifier PXD015502. Furthermore, the ratios between signaling proteins and the mean ± SD of the replicates belonging to the same animal are provided in Dataset Table EV1.

Processing of electron microscopy images

For the measurement of flagellar diameters and axonemal protein volumes, the following previously published cryo-electron tomography and subtomogram averaging data were used: the three-dimensional (3D) reconstructions of intact wild-type *Chlamydomonas reinhardtii* and sperm flagella from the sea urchin *Strongylocentrotus purpuratus* (Lin & Nicastro, 2018) for flagellar diameter, the 3D structures of the averaged DMT-associated (Lin *et al*, 2019) and central pair complex repeats (preprint: Fu *et al*, 2019) of wild-type *Chlamydomonas*, as well as the averaged DMT-associated repeats (Lin & Nicastro, 2018), and central pair complex repeats of sea urchin sperm flagella (Carbajal-Gonzalez *et al*, 2013).

The IMOD software (Kremer *et al*, 1996) and ImageJ (Schneider *et al*, 2012) were used for visualization of the tomographic slices and measurement of the diameters (measured at the inside of the flagellar membrane), respectively. Only tomograms with straight and non- or mildly compressed flagella were used for diameter measurements. In total, 6 tomograms of *Chlamydomonas* flagella and 19 tomograms of sea urchin sperm flagella were selected, and their diameters were measured at three different positions: proximal end, midpoint, and distal end.

The UCSF chimera package (Pettersen *et al*, 2004) was used for estimating the volumes occupied by axonemal proteins using the subtomogram averages of the 96-nm DMT-associated repeat (V_{DMT}) and the [3 × 32 nm] central pair complex repeat (V_{CPC}). The isosurface-rendering threshold for volume measurements was determined using the average density of 1.43 g/cm³ (Quillin & Matthews, 2000) for proteins and normalizing the threshold so that the measured molecular mass of microtubule protofilaments and dynein heads matched the calculated molecular masses for a 96-nm long protofilament (~1,200 kDa) and dynein head domain (~350 kDa). For instance, the surface threshold for the averaged 96-nm DMT-associated axonemal repeat of *Chlamydomonas* was set to 125.1, resulting in estimated molecular weights for the IDA *a* dynein head and protofilament B7 of 343 and 1,210 kDa, respectively.

Volume calculations

The measured average diameters ($d = 2r$) of the *Chlamydomonas* and sea urchin sperm flagella were used to calculate the total volumes V_t for a flagellar length (l) as $V_t = \pi \times r^2 \times l$. The volumes of the axonemal proteins were calculated for 96-nm length as $V_a = (9 \times V_{DMT}) + V_{CPC}$ and then scaled to 1-µm flagellar length. For measuring the luminal volumes V_l inside the DMTs and central pair microtubules, we "filled" the microtubule lumen in the subtomogram averages of the 96-nm DMT-associated repeat and the [3 × 32 nm] central pair complex repeat by setting the pixel values inside the microtubules to zero (i.e., black like protein) using a mask or the IMOD command imodmop. Using the same chimera thresholds as for estimating the volumes V_{DMT} and V_{CPC} before, we estimated the volumes of the "filled" averages V^*_{DMT} and V^*_{CPC} and calculated $V_l = (9 \times V^*_{DMT}) + V^*_{CPC} - V_a$ for 96-nm length, which was then scaled to 1-µm flagellar length.
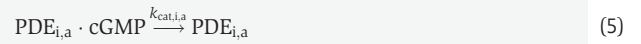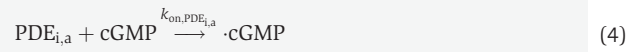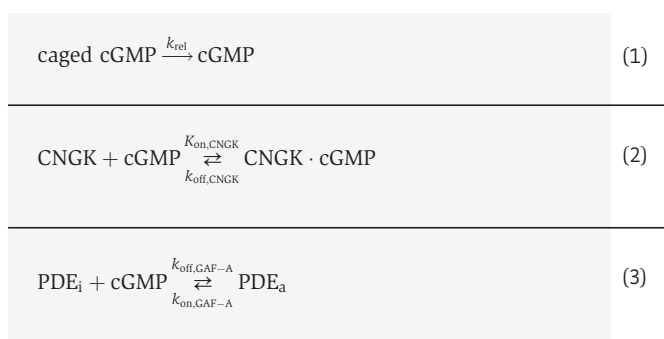
Stopped-flow techniques

Resact- and cGMP-induced changes in membrane voltage were measured with a voltage-sensitive dye (FluoVolt, Thermo Fisher) in a stopped-flow device (SFM-400; Bio-Logic) as described previously (Hamzeh et al, 2019). Dry sperm was suspended 1:6 (v/v) in loading buffer containing ASW and 5 µM fluorescent dye. After incubation for at least 20 min at 18 °C, the sample was diluted 1:20 with ASW in the presence of 15 µM caged DEACM-cGMP and 0.05% Pluronic F127 (Sigma-Aldrich). In the stopped-flow device, sperm were rapidly mixed 1:1 with either ASW or ASW containing 191 mM K^+. Mixing with 191 mM K^+ ASW yielded a final K^+ concentration of 100 mM (referred to as 100KASW). Fluorescence was excited by a Spectra X Light Engine (Lumencor). Emission was recorded by photomultiplier modules (H9656-20; Hamamatsu Photonics). Data acquisition was performed with a data acquisition board (PCI-6221; National Instruments) and Bio-Kine software v. 4.49 (Bio-Logic). The excitation light was passed through a BrightLine 513/17 nm filter (Semrock). The excitation light was operated at 1–10 kHz. Emission was recorded through a 542/20 nm filter by a photomultiplier module and filtered through a lock-in amplifier. Signals represent the average of at least two recordings and are depicted as the percent change in fluorescence (ΔF) relative to the mean of the first 5–10 data points before the onset of the signal (F_o). The control (ASW) $\Delta F/F_o$ signal was subtracted from the resact- or cGMP-induced signals. The data obtained were analyzed and plotted using OriginPro 9.0 (OriginLab Corporation).

Caged compounds and flash photolysis

Caged cGMP was photolyzed using a 365-nm LED (M365LP1, Thorlabs). The LED was coupled to a liquid light guide and delivered to the cuvette (FC-15 Bio-Logic). The fluorescence background resulting from the 365-nm LED was removed using lock-in detection. The waveform, timing, and triggering of the photolysis light were controlled through the interface of a self-made LabVIEW program using a DAQ card (NIUSB-625; National Instruments). The photolytic release of cGMP was calibrated via the increase in fluorescence upon photolysis (Hamzeh et al, 2019).

Data analysis and simulations

Simulations of cGMP dynamics in the flagellum were based on the following reaction schemes:

$$\text{caged cGMP} \xrightarrow{k_{rel}} \text{cGMP} \tag{1}$$

$$\text{CNGK} + \text{cGMP} \underset{k_{off,CNGK}}{\overset{K_{on,CNGK}}{\rightleftarrows}} \text{CNGK} \cdot \text{cGMP} \tag{2}$$

$$\text{PDE}_i + \text{cGMP} \underset{k_{on,GAF-A}}{\overset{k_{off,GAF-A}}{\rightleftarrows}} \text{PDE}_a \tag{3}$$

$$\text{PDE}_{i,a} + \text{cGMP} \xrightarrow{k_{on,PDE_{i,a}}} \cdot \text{cGMP} \tag{4}$$

$$\text{PDE}_{i,a} \cdot \text{cGMP} \xrightarrow{k_{cat,i,a}} \text{PDE}_{i,a} \tag{5}$$

These reactions correspond to the release of cGMP from its caged derivative (reaction 1), binding (unbinding) of cGMP to (from) the CNGK channel (reaction 2), binding (unbinding) of cGMP to (from) the allosteric GAF-A domain of the inactive PDE (PDE$_i$) to produce active PDE (PDE$_a$; reaction 3), cGMP binding to the catalytic domain of PDE of either PDE$_i$ or PDE$_a$ (PDE$_{i,a}$) (reaction 4), and cGMP hydrolysis by PDE (reaction 5). Reaction rates were taken from previous studies (see Appendix Table S3). The catalytic rate for hydrolysis (k_{cat}) of cGMP by PDE$_i$ is assumed to be about one-third of that of PDE$_a$, as reported for mammalian PDE5 (Rybalkin et al, 2003). The apparent k_{on} for cGMP binding to the catalytic domain of PDE (reaction 4) was estimated assuming that the reaction is irreversible (k_{off} ~0/s), and using the Michaelis–Menten relation: $K_M = (k_{off} + k_{cat})/k_{on}$, wherein K_M is the Michaelis–Menten constant. The maximal catalytic rate (k_{cat}) was estimated from cGMP measurements of sperm stimulated with saturating resact concentrations (Appendix) (Kaupp et al, 2003).

Discrete-event simulations were performed using the direct Gillespie method (Gillespie, 1977). Stochastic reaction rates were derived from the deterministic rates listed in Appendix Table S3. The on rates for the second-order reactions 2, 3, and 4 were normalized by the flagellar volume as described (Gillespie, 1977). The flagellum was approximated by a cylinder 40 µm in length and a radius of 125 nm. Turnover rates were obtained by fitting of a mono-exponential decay function to the average of 100 simulations.

Fitting of depolarizing V_m signals

Depolarization signals resulting from 2-ms flashes in the presence of 100KASW were fitted with the equation:

$$V_m(t) = A(1 - e^{-t/\tau_{rise}})e^{-t/\tau_{relax}} \tag{1}$$

Estimate of time constant of cGMP binding

The time constant of cGMP binding to CNGK was calculated using:

$$\tau_{on} = \frac{1}{k_{on}[\text{CNGK}]} \tag{2}$$

Fitting of light-evoked V_m responses

A macroscopic heuristic model was used for fitting voltage data. The change in free cGMP concentration ([cGMP]) was derived for the mass-balance equation:

$$\frac{d[\text{cGMP}]}{dt} = k_{rel} - k_{on,PDE}[\text{cGMP}][\text{PDE}] - k_{on,CNGK}[\text{cGMP}][\text{CNGK}]$$
$$+ k_{off,CNGK}[\text{CNGK} \cdot \text{cGMP}] \tag{3}$$

where in k_{rel} represents the rate of cGMP release by light and [PDE], [PDE·cGMP], and [CNGK·cGMP] are the free concentrations of PDE, PDE bound to cGMP, and CNGK bound to cGMP,

respectively. For simplicity, we assume that [CNGK·cGMP] and V_m are proportional to [cGMP] and that binding of cGMP to PDE is irreversible. Additionally, for low light levels, [PDE] and [CNGK] can be approximated by a constant.

Equation (3) was solved for a square pulse stimulation (Fig 3C). All fits were performed using nonlinear least-square methods. For a square release waveform, the release rate can be approximated by

$$k_{\mathrm{rel}} = \begin{cases} k & t_{\mathrm{on}} < t < t_{\mathrm{off}} \\ 0 & \text{otherwise} \end{cases}, \tag{4}$$

where in k is a constant and t_{on} and t_{off} correspond to the time points where the UV light was switched on and off, respectively. Solving equation (3) yields the following:

$$V_{rmm} = \begin{cases} A(1 - e^{-\mathrm{keff} \cdot t}) & t_{\mathrm{on}} < t < t_{\mathrm{off}} \\ A e^{-\mathrm{keff} \cdot t} & \text{otherwise} \end{cases}, \tag{5}$$

with A and k_{eff} being constants.

Time constant of cGMP binding to CNGK

The time constant of cGMP binding to the CNGK channel was estimated to be between 1 and 2 ms (equation 2) using a lower and upper bounds of k_{on}. A $k_{\mathrm{on}} = 2.6 \times 10^7$/M/s was determined for a CNBD of similar affinity (Peuker *et al*, 2012). The k_{on} is moderately dependent on ionic strength; it is maximally twofold larger at the high ionic strength of ASW compared with a Ringer solution (Peuker *et al*, 2012). CNGK concentration is 21.6 μM. This exercise shows that cGMP binding is at least an order of magnitude faster than τ_{rise} of cGMP-induced ΔV_m.

Estimate of membrane time constant

The τ_{RC} of sperm was estimated to be 5–20 ms assuming an input resistance of mouse sperm of about 10–20 GΩ (Navarro *et al*, 2007; Zeng *et al*, 2013). As membrane capacitance, we used $C_m = 1$ pF. In mouse, C_m was measured to be 2.5 pF (Navarro *et al*, 2007). Thus, the C_m is estimated to be 1.25 pF in sea urchin sperm, i.e., half of the value measured in mouse sperm, whose flagellum is about twofold longer (100 μm) than that of *A. punctulata* sperm. The time constant of CNGK activation is not known, but is of the order of a few milliseconds for ion channels (Hille, 2004). Thus, τ_{rise} of cGMP-induced ΔV_m agrees well with these estimates.

Estimate of the rate of cGMP by PDE5

The rate k_{cat} for PDE5 was estimated based on previous studies where the cGMP kinetics was evaluated by quench-flow techniques on intact sperm. In brief, sperm were mixed with saturating resact concentrations (250 nM) and the suspension was allowed to age. After different time intervals, the suspension was mixed with a denaturing agent (perchloric acid) stopping all biological reactions, and the cGMP concentration in the cell was determined using a radioimmunoassay (Kaupp *et al*, 2003). The total cGMP synthesized could be estimated from experiments performed in the presence of the PDE5 inhibitor IBMX to be about 110 pmol cGMP per 10^8 cells, i.e., about 6.6×10^5 cGMP molecules per sperm cell (or 660 μM), assuming a flagellar volume of 1.7 fl. At such high cGMP concentrations, all binding domains for cGMP are fully saturated. From the time difference between synthesis and total cGMP(t) in the cell, a hydrolysis rate of about 40 pmol cGMP per 10^8 cells in 0.2 s can be derived. This rate is equivalent to a k_{cat} of 24/s. This rate is larger than that observed for mammalian PDE5 (approximately 4/s) (Francis & Corbin, 2010). Of note, this estimate for k_{cat} could underestimate the catalytic rate of the sea urchin PDE5, if enzyme inhibition by IBMX was incomplete.

Single-cell Ca²⁺ and pH_i measurements

Sperm cells were suspended 1:100 (v/v) in ASW supplemented with 0.5% Pluronic F127 (Sigma-Aldrich) and either 30 μM GFP-certified FluoForte-AM (Enzo Life Sciences; Ca^{2+} imaging) or 20 μM pHrodo Red (Molecular Probes; pH imaging). Samples were incubated for 45 min at room temperature; 10 min prior to the measurements, DEACM-caged cGMP (15 μM) was included in the incubation. Fluorescence was recorded from single cells with an inverted microscope (Olympus IX71) equipped with a 20× objective lens (UPlanSApo 20×, 0.75 NA; Olympus) and two dichroic mirrors to image sperm that were loaded with GFP-certified FluoForte (520LP; FF520-Di02; Semrock) or pHrodo Red (560 DCXR; Chroma). For sharp imaging of the rapidly moving sperm flagellum, 2-ms pulses of excitation light were used (Spectra X Light Engine; Lumencor). For Ca^{2+} imaging, Teal light was used in combination with the excitation band-pass filter (513/17; FF01-513/17; Semrock) and a long-pass filter (BLP01-532R; Semrock). Due to the large difference in emission intensity between head and flagellum, imaging with pHrodo Red resulted either in a poor dynamical range for imaging of the flagellum or in a saturating head signal. To overcome this problem, we used two alternating excitation wavelengths with different pHrodo Red excitation efficacies: Green excitation (Spectra X Light Engine; Lumencor) in combination with a band-pass excitation filter (ET545/30; Chroma) was used to image the sperm flagellum, and Teal excitation (Spectra X Light Engine; Lumencor) in combination with an excitation filter (FF01-513/17 nm; Semrock) for imaging of the head. Emission light from pHrodo Red was filtered using a band-pass filter (BA575-625; Olympus). Emitted light was collected using a back-illuminated electron-multiplying charge-coupled device camera (DU-897D; Andor Technology). Photolysis of DEACM-caged cGMP was accomplished with either 365 nm LED (10 ms flashes; M365LP1, Thorlabs) or the 390-nm LED from the Spectra X Light Engine (20-ms flashes; Lumencor). Quantification of fluorescence signals was done using custom-made software written in MATLAB (MathWorks) (Alvarez *et al*, 2012). Signal smoothing was done using a moving average of three points, corresponding to a time window of 208 ms (pH imaging) or 107 ms (Ca^{2+} imaging).

Data availability

Shotgun proteomics data have been uploaded to PRIDE with identifier PXD015332, http://www.ebi.ac.uk/pride/archive/projects/PXD015332. Targeted proteomics data can be accessed at PRIDE with identifier PXD015502 and PANORAMA with URL https://panoramaweb.org/arbacia_flagella.url.

Expanded View for this article is available online.

Acknowledgements

Author contributions

UBK, CT, HH, LA, RS, and TS contributed to the design of the project; CT and AP performed and analyzed mass spectrometry experiments; HH, UBK, TS, and RS performed stopped-flow experiments; WB performed sequence analysis; HGK and AM prepared and characterized flagella preparations; LA designed and programmed numerical simulation; LA, FL, and RP performed Ca^{2+} and pH measurements on single cells; AR synthesized all caged compounds; DN and LG determined the flagellar volumes from cryo-tomograms; UBK, HH, LA, RS, DN, and AP wrote the manuscript. All authors edited the manuscript. The authors declare no competing financial interests.

Conflict of interest

The authors declare that they have no conflict of interest.

References

Adlung L, Kar S, Wagner MC, She B, Chakraborty S, Bao J, Lattermann S, Boerries M, Busch H, Wuchter P *et al* (2017) Protein abundance of AKT and ERK pathway components governs cell type-specific regulation of proliferation. *Mol Syst Biol* 13: 904

Alvarez L, Dai L, Friedrich BM, Kashikar ND, Gregor I, Pascal R, Kaupp UB (2012) The rate of change in Ca^{2+} concentration controls sperm chemotaxis. *J Cell Biol* 196: 653–663

Balbach M, Beckert V, Hansen JN, Wachten D (2018) Shedding light on the role of cAMP in mammalian sperm physiology. *Mol Cell Endocrinol* 468: 111–120

Barrow AJ, Wu SM (2009) Low-conductance HCN1 ion channels augment the frequency response of rod and cone photoreceptors. *J Neurosci* 29: 5841–5853

Baylor DA, Lamb TD, Yau K-W (1979) Responses of retinal rods to single photons. *J Physiol* 288: 613–634

Beltrán C, Vacquier VD, Moy G, Chen Y, Buck J, Levin LR, Darszon A (2007) Particulate and soluble adenylyl cyclases participate in the sperm acrosome reaction. *Biochem Biophys Res Commun* 358: 1128–1135

Berg HC, Purcell EM (1977) Physics of chemoreception. *Biophys J* 20: 193–219

Berg HC (1993) *Random walks in biology*. Princeton, NJ: Princeton University Press

Boland W, Terlinden R, Jaenicke L, Muller DG (1982) Binding-mechanism and sensitivity in gamete chemotaxis of the phaeophyte *Cutleria multifida*. *Eur J Biochem* 126: 173–179

Bönigk W, Loogen A, Seifert R, Kashikar N, Klemm C, Krause E, Hagen V, Kremmer E, Strünker T, Kaupp UB (2009) An atypical CNG channel activated by a single cGMP molecule controls sperm chemotaxis. *Sci Signal* 2: ra68

Breslow DK, Koslover EF, Seydel F, Spakowitz AJ, Nachury MV (2013) An *in vitro* assay for entry into cilia reveals unique properties of the soluble diffusion barrier. *J Cell Biol* 203: 129–147

Brownridge P, Holman SW, Gaskell SJ, Grant CM, Harman VM, Hubbard SJ, Lanthaler K, Lawless C, O'Cualain R, Sims P *et al* (2011) Global absolute quantification of a proteome: challenges in the deployment of a QconCAT strategy. *Proteomics* 11: 2957–2970

Buffone MG (2016) *Sperm acrosome biogenesis and function during fertilization*. New York, NY: Springer

Carbajal-Gonzalez BI, Heuser T, Fu X, Lin J, Smith BW, Mitchell DR, Nicastro D (2013) Conserved structural motifs in the central pair complex of eukaryotic flagella. *Cytoskeleton* 70: 101–120

Cervetto L, Lagnado L, Perry RJ, Robinson DW, McNaughton PA (1989) Extrusion of calcium from rod outer segments is driven by both sodium and potassium gradients. *Nature* 337: 740–743

Chung JJ, Navarro B, Krapivinsky G, Krapivinsky L, Clapham DE (2011) A novel gene required for male fertility and functional CATSPER channel formation in spermatozoa. *Nat Commun* 2: 153

Chung JJ, Miki K, Kim D, Shim SH, Shi HF, Hwang JY, Cai X, Iseri Y, Zhuang X, Clapham DE (2017) CatSperzeta regulates the structural continuity of sperm Ca^{2+} signaling domains and is required for normal fertility. *Elife* 6: e23082

Corbit KC, Aanstad P, Singla V, Norman AR, Stainier DY, Reiter JF (2005) Vertebrate Smoothened functions at the primary cilium. *Nature* 437: 1018–1021

DeCaen PG, Delling M, Vien TN, Clapham DE (2013) Direct recording and molecular identification of the calcium channel of primary cilia. *Nature* 504: 315–318

Delling M, DeCaen PG, Doerner JF, Febvay S, Clapham DE (2013) Primary cilia are specialized calcium signalling organelles. *Nature* 504: 311–314

Endres RG, Wingreen NS (2008) Accuracy of direct gradient sensing by single cells. *Proc Natl Acad Sci USA* 105: 15749–15754

Espinal-Enriquez J, Priego-Espinosa DA, Darszon A, Beltran C, Martinez-Mekler G (2017) Network model predicts that CatSper is the main Ca^{2+} channel in the regulation of sea urchin sperm motility. *Sci Rep* 7: 4236

Fain GL, Quandt FN, Bastian BL, Gerschenfeld HM (1978) Contribution of a caesium-sensitive conductance increase to the rod photoresponse. *Nature* 272: 467–469

Farci D (2017) Spatial organization of a chemoreceptor guanylate cyclase in the flagellum of *Arbacia punctulata* sperm. *University of Cologne*. PhD Thesis

Fischer F, Poetsch A (2006) Protein cleavage strategies for an improved analysis of the membrane proteome. *Proteome Sci* 4: 2

Francis SH, Corbin JD (2010) *Handbook of cell signaling*. Amsterdam, The Netherlands: Elsevier

Francis SH, Blount MA, Corbin JD (2011) Mammalian cyclic nucleotide phosphodiesterases: molecular mechanisms and physiological functions. *Physiol Rev* 91: 651–690

Fu G, Zhao L, Dymek E, Hou Y, Song K, Phan N, Shang Z, Smith EF, Witman GB, Nicastro D (2019) Structural organization of the C1a-e-c supercomplex within the ciliary central apparatus. *bioRxiv* https://doi.org/10.1101/773416 [PREPRINT]

Galindo BE, Neill AT, Vacquier VD (2005) A new hyperpolarization-activated, cyclic nucleotide-gated channel from sea urchin sperm flagella. *Biochem Biophys Res Commun* 334: 96–101

Galindo BE, de la Vega-Beltrán JL, Labarca P, Vacquier VD, Darszon A (2007) Sp-tetraKCNG: a novel cyclic nucleotide gated K$^+$ channel. *Biochem Biophys Res Commun* 354: 668–675

Garbers DL (1976) Sea urchin sperm guanylate cyclase. *J Biol Chem* 251: 4071–4077

Gauss R, Seifert R, Kaupp UB (1998) Molecular identification of a hyperpolarization-activated channel in sea urchin sperm. *Nature* 393: 583–587

Gillespie DT (1977) Exact stochastic simulation of coupled chemical reactions. *J Phys Chem* 81: 2340–2361

Gross OP, Pugh EN Jr, Burns ME (2015) cGMP in mouse rods: the spatiotemporal dynamics underlying single photon responses. *Front Mol Neurosci* 8: 6

Guerrero A, Espinal J, Wood CD, Rendon JM, Carneiro J, Martinez-Mekler G, Darszon A (2013) Niflumic acid disrupts marine spermatozoan chemotaxis without impairing the spatiotemporal detection of chemoattractant gradients. *J Cell Sci* 126: 1477–1487

Gunaratne HJ, Neill AT, Vacquier VD (2006) Plasma membrane calcium ATPase is concentrated in the head of sea urchin spermatozoa. *J Cell Physiol* 207: 413–419

Hagen V, Frings S, Wiesner B, Helm S, Kaupp UB, Bendig J (2003) [7-(Dialkylamino)coumarin-4-yl]methyl-caged compounds as ultrafast and effective long-wavelength phototriggers of 8-bromo-substituted cyclic nucleotides. *Chem Biol Chem* 4: 434–442

Halls ML, Canals M (2018) Genetically encoded FRET biosensors to illuminate compartmentalised GPCR signalling. *Trends Pharmacol Sci* 39: 148–157

Hamzeh H, Alvarez L, Strünker T, Kierzek M, Brenker C, Deal PE, Miller EW, Seifert R, Kaupp UB (2019) Kinetic and photonic techniques to study chemotactic signaling in sea urchin sperm. *Methods Cell Biol* 151: 487–517

Hansbrough JR, Garbers DL (1981) Sodium-dependent activation of sea urchin spermatozoa by speract and monensin. *J Biol Chem* 256: 2235–2241

Harumi T, Hoshino K, Suzuki N (1992) Effects of sperm-activating peptide I on *Hemicentrotus pulcherrimus* spermatozoa in high potassium sea water. *Dev Growth Differ* 34: 163–172

Hille B (2004) *Ionic channels of excitable membranes*. Sunderland, MA: Sinauer Associates

Holman SW, Sims PF, Eyers CE (2012) The use of selected reaction monitoring in quantitative proteomics. *Bioanalysis* 4: 1763–1786

Jalloul AH, Szerencsei RT, Schnetkamp PP (2016) Cation dependencies and turnover rates of the human K^+-dependent Na^+-Ca^{2+} exchangers NCKX1, NCKX2, NCKX3 and NCKX4. *Cell Calcium* 59: 1–11

Kaissling KE (1986) Chemo-electrical transduction in insect olfactory receptors. *Annu Rev Neurosci* 9: 121–145

Kambara Y, Shiba K, Yoshida M, Sato C, Kitajima K, Shingyoji C (2011) Mechanism regulating Ca^{2+}-dependent mechanosensory behaviour in sea urchin spermatozoa. *Cell Struct Funct* 36: 69–82

Kaupp UB, Seifert R (2002) Cyclic nucleotide-gated ion channels. *Physiol Rev* 82: 769–824

Kaupp UB, Solzin J, Hildebrand E, Brown JE, Helbig A, Hagen V, Beyermann M, Pampaloni F, Weyand I (2003) The signal flow and motor response controling chemotaxis of sea urchin sperm. *Nat Cell Biol* 5: 109–117

Kaupp UB, Alvarez L (2016) Sperm as microswimmers - navigation and sensing at the physical limit. *Eur Phys J Special Topics* 225: 2119–2139

Kaupp UB, Strünker T (2017) Signaling in sperm: more different than similar. *Trends Cell Biol* 27: 101–109

Kee HL, Dishinger JF, Blasius TL, Liu CJ, Margolis B, Verhey KJ (2012) A size-exclusion permeability barrier and nucleoporins characterize a ciliary pore complex that regulates transport into cilia. *Nat Cell Biol* 14: 431–437

Kremer JR, Mastronarde DN, McIntosh JR (1996) Computer visualization of three-dimensional image data using IMOD. *J Struct Biol* 116: 71–76

Krishnamurthy S, Moorthy BS, Xin Xiang L, Xin Shan L, Bharatham K, Tulsian NK, Mihalek I, Anand GS (2014) Active site coupling in PDE:PKA complexes promotes resetting of mammalian cAMP signaling. *Biophys J* 107: 1426–1440

Krishnamurthy S, Tulsian NK, Chandramohan A, Anand GS (2015) Parallel allostery by cAMP and PDE coordinates activation and termination phases in cAMP signaling. *Biophys J* 109: 1251–1263

Lee HC (1985) The voltage-sensitive Na^+/H^+ exchange in sea urchin spermatozoa flagellar membrane vesicles studied with an entrapped pH probe. *J Biol Chem* 260: 10794–10799

Leinders-Zufall T, Lane AP, Puche AC, Ma W, Novotny MV, Shipley MT, Zufall F (2000) Ultrasensitive pheromone detection by mammalian vomeronasal neurons. *Nature* 405: 792–796

Lin J, Nicastro D (2018) Asymmetric distribution and spatial switching of dynein activity generates ciliary motility. *Science* 360: eaar1968

Lin J, Le TV, Augspurger K, Tritschler D, Bower R, Fu G, Perrone C, O'Toole ET, Mills KV, Dymek E *et al* (2019) FAP57/WDR65 targets assembly of a subset of inner arm dyneins and connects to regulatory hubs in cilia. *Mol Biol Cell* 30: 2659–2680

Liu J, Xia J, Cho KH, Clapham DE, Ren D (2007) CatSperbeta, a novel transmembrane protein in the CatSper channel complex. *J Biol Chem* 282: 18945–18952

Luo DG, Yue WW, Ala-Laurila P, Yau KW (2011) Activation of visual pigments by light and heat. *Science* 332: 1307–1312

MacLean B, Tomazela DM, Shulman N, Chambers M, Finney GL, Frewen B, Kern R, Tabb DL, Liebler DC, MacCoss MJ (2010) Skyline: an open source document editor for creating and analyzing targeted proteomics experiments. *Bioinformatics* 26: 966–968

Marshall W, Basto R (2017) *Cilia*. Cold Spring Harbor, NY: Cold Spring Harbor Perspectives in Biology

Mick DU, Rodrigues RB, Leib RD, Adams CM, Chien AS, Gygi SP, Nachury MV (2015) Proteomics of primary cilia by proximity labeling. *Dev Cell* 35: 497–512

Miller EW, Lin JY, Frady EP, Steinbach PA, Kristan WB Jr, Tsien RY (2012) Optically monitoring voltage in neurons by photo-induced electron transfer through molecular wires. *Proc Natl Acad Sci USA* 109: 2114–2119

Moore BS, Stepanchick AN, Tewson PH, Hartle CM, Zhang J, Quinn AM, Hughes TE, Mirshahi T (2016) Cilia have high cAMP levels that are inhibited by Sonic Hedgehog-regulated calcium dynamics. *Proc Natl Acad Sci USA* 113: 13069–13074

Mukherjee S, Jansen V, Jikeli JF, Hamzeh H, Alvarez L, Dombrowski M, Balbach M, Strünker T, Seifert R, Kaupp UB *et al* (2016) A novel biosensor to study cAMP dynamics in cilia and flagella. *Elife* 5: e14052

Mukhopadhyay S, Rohatgi R (2014) G-protein-coupled receptors, Hedgehog signaling and primary cilia. *Semin Cell Dev Biol* 33: 63–72

Navarro B, Kirichok Y, Clapham DE (2007) KSper, a pH-sensitive K^+ current that controls sperm membrane potential. *Proc Natl Acad Sci USA* 104: 7688–7692

Navarro B, Kirichok Y, Chung JJ, Clapham DE (2008) Ion channels that control fertility in mammalian spermatozoa. *Int J Dev Biol* 52: 607–613

Pan B, Akyuz N, Liu XP, Asai Y, Nist-Lund C, Kurima K, Derfler BH, Gyorgy B, Limapichat W, Walujkar S *et al* (2018) TMC1 forms the pore of mechanosensory transduction channels in vertebrate inner ear hair cells. *Neuron* 99: 736–753 e736

Pape H-C (1996) Queer current and pacemaker: the hyperpolarization-activated cation current in neurons. *Annu Rev Physiol* 58: 299–327

Perez-Riverol Y, Csordas A, Bai J, Bernal-Llinares M, Hewapathirana S, Kundu DJ, Inuganti A, Griss J, Mayer G, Eisenacher M *et al* (2019) The PRIDE database and related tools and resources in 2019: improving support for quantification data. *Nucleic Acids Res* 47: D442–D450

Pettersen EF, Goddard TD, Huang CC, Couch GS, Greenblatt DM, Meng EC, Ferrin TE (2004) UCSF Chimera—a visualization system for exploratory research and analysis. *J Comput Chem* 25: 1605−1612

Peuker S, Cukkemane A, Held M, Noe F, Kaupp UB, Seifert R (2012) Kinetics of ligand-receptor interaction reveals an induced-fit mode of binding in a cyclic nucleotide-activated protein. *Biophys J* 104: 63−73

Pichlo M, Bungert-Plümke S, Weyand I, Seifert R, Bönigk W, Strünker T, Kashikar ND, Goodwin N, Müller A, Pelzer P *et al* (2014) High density and ligand affinity confer ultrasensitive signal detection by a guanylyl cyclase chemoreceptor. *J Cell Biol* 206: 541−557

Postea O, Biel M (2011) Exploring HCN channels as novel drug targets. *Nat Rev Drug Discov* 10: 903−914

Quillin ML, Matthews BW (2000) Accurate calculation of the density of proteins. *Acta Crystallogr D Biol Crystallogr* 56: 791−794

Ramirez-Sarmiento CA (2017) "Riddle Me This": substrate channeling solves the paradigms of cAMP-dependent activation of PKA. *Biophys J* 112: 2451−2453

Rivers J, Simpson DM, Robertson DH, Gaskell SJ, Beynon RJ (2007) Absolute multiplexed quantitative analysis of protein expression during muscle development using QconCAT. *Mol Cell Proteomics* 6: 1416−1427

Rybalkin SD, Rybalkina IG, Shimizu-Albergine M, Tang XB, Beavo JA (2003) PDE5 is converted to an activated state upon cGMP binding to the GAF A domain. *EMBO J* 22: 469−478

Schneider CA, Rasband WS, Eliceiri KW (2012) NIH Image to ImageJ: 25 years of image analysis. *Nat Methods* 9: 671−675

Schnetkamp PP (2013) The SLC24 gene family of Na^+/Ca^{2+}-K^+ exchangers: from sight and smell to memory consolidation and skin pigmentation. *Mol Aspects Med* 34: 455−464

Schnetkamp PP, Jalloul AH, Liu G, Szerencsei RT (2014) The SLC24 family of K^+-dependent Na^+-Ca^{2+}-exchangers: structure-function relationships. *Curr Top Membr* 73: 263−287

Scott KB, Turko IV, Phinney KW (2016) QconCAT: internal standard for protein quantification. *Methods Enzymol* 566: 289−303

Seifert R, Flick M, Bönigk W, Alvarez L, Trötschel C, Poetsch A, Müller A, Goodwin N, Pelzer P, Kashikar ND *et al* (2015) The CatSper channel controls chemosensation in sea urchin sperm. *EMBO J* 34: 379−392

Singh S, Lowe DG, Thorpe DS, Rodriguez H, Kuang W-J, Dangott LJ, Chinkers M, Goeddel DV, Garbers DL (1988) Membrane guanylate cyclase is a cell-surface receptor with homology to protein kinases. *Nature* 334: 708−712

Starr RC, Marner FJ, Jaenicke L (1995) Chemoattraction of male gametes by a pheromone produced by female gametes of Chlamydomonas. *Proc Natl Acad Sci USA* 92: 641−645

Strünker T, Weyand I, Bönigk W, Van Q, Loogen A, Brown JE, Kashikar N, Hagen V, Krause E, Kaupp UB (2006) A K^+ -selective cGMP-gated ion channel controls chemosensation of sperm. *Nat Cell Biol* 8: 1149−1154

Su Y-H, Vacquier VD (2002) A flagellar K^+-dependent Na^+/Ca^{2+} exchanger keeps Ca^{2+} low in sea urchin spermatozoa. *Proc Natl Acad Sci USA* 99: 6743−6748

Su YH, Vacquier VD (2006) Cyclic GMP-specific phosphodiesterase-5 regulates motility of sea urchin spermatozoa. *Mol Biol Cell* 17: 114−121

Tulsian NK, Krishnamurthy S, Anand GS (2017) Channeling of cAMP in PDE-PKA complexes promotes signal adaptation. *Biophys J* 112: 2552−2566

Vacquier VD, Loza-Huerta A, Garcia-Rincon J, Darszon A, Beltran C (2014) Soluble adenylyl cyclase of sea urchin spermatozoa. *Biochim Biophys Acta* 1842: 2621−2628

Wachten D, Jikeli JF, Kaupp UB (2017) Sperm sensory signaling. *Cold Spring Harb Perspect Biol* 9: a028225

Wang D, King SM, Quill TA, Doolittle LK, Garbers DL (2003) A new sperm-specific Na^+/H^+ exchanger required for sperm motility and fertility. *Nat Cell Biol* 5: 1117−1122

Wang H, Liu J, Cho KH, Ren D (2009) A novel, single, transmembrane protein CATSPERG is associated with CATSPER1 channel protein. *Biol Reprod* 81: 539−544

Windler F, Bönigk W, Körschen HG, Grahn E, Strünker T, Seifert R, Kaupp UB (2018) The solute carrier SLC9C1 is a Na^+/H^+-exchanger gated by an S4-type voltage-sensor and cyclic-nucleotide binding. *Nat Comm* 9: 2809

Woodruff ML, Sampath AP, Matthews HR, Krasnoperova NV, Lem J, Fain GL (2002) Measurement of cytoplasmic calcium concentration in the rods of wild-type and transducin knock-out mice. *J Physiol* 542: 843−854

Yau KW, Hardie RC (2009) Phototransduction motifs and variations. *Cell* 139: 246−264

Zeng XH, Navarro B, Xia XM, Clapham DE, Lingle CJ (2013) Simultaneous knockout of Slo3 and CatSper1 abolishes all alkalization- and voltage-activated current in mouse spermatozoa. *J Gen Physiol* 142: 305−313

Zhao B, Müller U (2015) The elusive mechanotransduction machinery of hair cells. *Curr Opin Neurobiol* 34: 172−179

Zimmerman AL, Yamanaka G, Eckstein F, Baylor DA, Stryer L (1985) Interaction of hydrolysis-resistant analogs of cyclic GMP with the phosphodiesterase and light-sensitive channel of retinal rod outer segments. *Proc Natl Acad Sci USA* 82: 8813−8817